

The CLAS12 Ring Imaging Cherenkov Detector

M. Contalbrigo^a, V. Kubarovskiy^f, M. Mirazita^b, P. Rossi^{f,b}, G. Angelini^{b,j}, H. Avakian^f, K. Bailey^g, I. Balossino^a, L. Barion^a, F. Benmokhtar^h, P. Bonneau^f, W. Briscoe^j, W. Brooks^k, E. Cisbani^c, C. Cuevas^f, P. Degtarenko^f, C. Dickover^f, K. Hafidi^g, K. Jooⁱ, A. Kimⁱ, T. Lemon^f, V. Lucherini^b, R. Malagutti^a, R. Montgomery^b, A. Movsisyan^a, P. Musico^d, T. O'Connor^g, D. Orechini^b, L.L. Pappalardo^a, C. Pecar^h, R. Perrino^e, B. Raydo^f, S. Tomassini^b, M. Turisini^{a,b}, A. Yegneswaran^f

^aINFN Sezione di Ferrara and University of Ferrara, 44100 Ferrara, Italy

^bINFN Laboratori Nazionali di Frascati, 00044 Frascati, Italy

^cINFN Sezione di Roma1 - Gruppo Collegato Sanità and Italian National Institute of Health, 00153 Rome, Italy

^dINFN Sezione di Genova, 16146 Genova, Italy

^eINFN Sezione di Bari, 70126 Bari, Italy

^fThomas Jefferson National Accelerator Facility, Newport News, VA, 23606 USA

^gArgonne National Laboratory, Lemont, IL, 60439 USA

^hDuquesne University, Pittsburgh, PA, 15282 USA

ⁱUniversity of Connecticut, Storrs, CT, 06269 USA

^jThe George Washington University, Washington, DC, 20052 USA

^kUniversidad Técnica Federico Santa María, Casilla 110-V Valparaíso, Chile

Abstract

A Ring Imaging Cherenkov detector has been installed in the CLAS12 spectrometer at Jefferson Laboratory (JLab) to provide kaon identification in the momentum range between 3 and 8 GeV. The detector adopts a hybrid optics solution with aerogel radiator, light planar and spherical mirrors, and highly segmented photon detectors. We report here on the design, construction, and initial performance of the RICH during the commissioning of the detector and the first physics data taking period.

Keywords: Ring-imaging Cherenkov detectors, PID detectors, Single-photon detection

1. Overview

Particle identification (PID) of hadrons in the original baseline design of the Forward Detector of CLAS12 is obtained by combining the information from the High Threshold Cherenkov Counter (HTCC) [1], Low Threshold Cherenkov Counter (LTCC) [2], and Forward Time-of-Flight (FTOF) [3] systems. However, no sufficient separation of kaons from pions and protons can be achieved by using only these detectors in the momentum range relevant for the approved semi-inclusive deep inelastic scattering (SIDIS) physics program, i.e. between 3 and 8 GeV. Therefore, improved particle identification in this momentum range is achieved by replacing two sectors of the existing LTCC with Ring Imaging Cherenkov (RICH) detectors. The first module of the RICH detector was completed before the start of the physics run, see Fig. 1, while the installation of the second module in the opposite sector is foreseen for the beginning of the CLAS12 operation with polarized targets. This article reports on the design, construction, and initial performance of the first RICH module. The second module will be identical to the first one.

The idea of a RICH detector is based on the fact that when a fast particle crosses a radiator with a velocity β

larger than the velocity of the light in that medium, it generates Cherenkov radiation. The light is emitted in a cone with opening angle θ_C given by $\cos(\theta_C) = [\beta n(\lambda)]^{-1}$, where $n(\lambda)$ is the refractive index of the radiator, which may depend on the wavelength λ . After a gap region where the cone opens up, the photons are detected and the ring can be reconstructed. A precision measurement of the Cherenkov angle provides the velocity of the particle and, together with information from the tracking system, it allows its identification. Thus, the capability of identify particles with a known momentum and different velocity is governed by the Cherenkov angle resolution, and it can be effectively parameterized by the separation in units of resolution n_σ between the angle distributions for the various particles.

2. The RICH Detector Requirements and Design

The CLAS12 spectrometer in Hall B [4] is designed to operate with highly polarized beams and nucleon targets at a luminosity of $10^{35} \text{ cm}^{-2}\text{s}^{-1}$. Under these conditions the production rate of protons, kaons, and pions studied using SIDIS Monte Carlo event-lists is such that, in most of the kinematic plane, the kaon rate is about one order of magnitude lower than the rate of pions and protons.



Figure 1: The first module of the CLAS12 RICH installed in Sector 4 of the Hall B Forward Carriage.

48 Thus, successful kaon identification requires a rejection
 49 factor from pions around 1:500, i.e. a contamination in
 50 the kaon sample of a few percent. This corresponds to
 51 4σ separation. In the momentum range between 3 and 82
 52 GeV, neither gas nor liquid radiators provide sufficient 83
 53 angular separation to achieve the required pion rejection 84
 54 factor (see Fig. 2) and the only viable solution is silica 85
 55 aerogel, an amorphous solid network of SiO_2 nanocrystals 86
 56 with a very low macroscopic density and a refractive index 87
 57 in between gases and liquids. 88

58 To detect the Cherenkov light emitted in the visible 89
 59 wavelength range, Hamamatsu Multi-Anode PhotoMul- 90
 60 tipliers Tubes (MaPMTs) were chosen for their high 91
 61 quantum efficiency in the visible and near ultraviolet 92
 62 (UV) regions, their fast response, and the required spatial 93
 63 resolution. Since the RICH detector must fit into the 94
 64 original CLAS12 Forward Carriage, there were several 95
 65 constraints imposed upon its design. Each sector required 96
 66 a projective geometry, limited depth of 1.2 m, and 97
 67 $\sim 4.5 \text{ m}^2$ entrance windows. Simulation studies favored a 98
 68 hybrid imaging Cherenkov detector design incorporating 99
 69 aerogel radiators, visible light photon detectors, and a¹⁰⁰
 70 focusing mirror system. The focusing mirror system¹⁰¹
 71 is used to reduce the detection area instrumented by¹⁰²
 72 the photon detectors to $\sim 1 \text{ m}^2$ per sector, minimizing¹⁰³
 73 costs and influence on the FTOF and Electromagnetic¹⁰⁴
 74 Calorimeter [5] systems. Depending upon the incident¹⁰⁵
 75 particle track angle, Cherenkov light is either imaged¹⁰⁶
 76 directly or after one or more reflections and passes through¹⁰⁷
 77 the aerogel. Figure 3 shows a schematic view of two¹⁰⁸
 78 examples of direct imaging and imaging after multiple¹⁰⁹
 79 reflections. Such a peculiar hybrid-optics design is an¹¹⁰
 80 innovative solution that has been successfully validated¹¹¹
 81 with a test-beam campaign [6]. 112

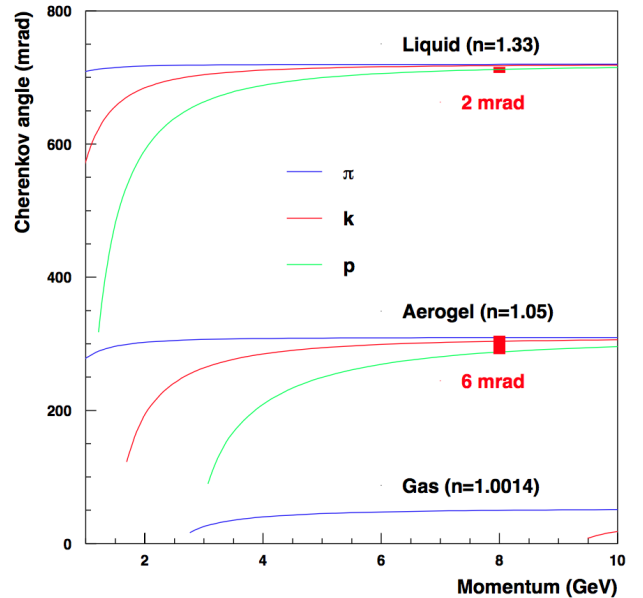


Figure 2: Cherenkov light opening angle as a function of the momentum for different particles using liquid, gas, or aerogel radiators. The angular separation between kaons and pions at the highest momenta is also indicated.

The RICH detector replaces two sectors of the existing gas Low Threshold Cherenkov detector (LTCC), which is located at a 5-m distance from the beam-target interaction point. The first RICH module was designed while the CLAS12 spectrometer was already under construction and, as a consequence, it had to cover the same large area to match the trapezoidal shape of the LTCC sector. This resulted in several challenging requirements for the mechanical structure. The guiding principles were to minimize the material budget inside the acceptance and to limit the impact on the downstream detectors, ensuring at the same time the rigidity of the structure imposed by the optical requirements. Therefore, light materials, in particular carbon fiber, were largely utilized for all elements inside the CLAS12 acceptance. For all the parts with large dimensions, the sandwich technique, in which two thin solid skins are glued together on a thick honeycomb core, was also used. This technique indeed combines high stiffness with substantial weight reduction, resulting in a total weight of the detector of about 900 kg, $\sim 30\%$ lower than the LTCC.

A sketch of the detector is shown in Fig. 4. It is composed of a trapezoidal box (larger base of 4.2 m, smaller base of 0.3 m, height of 3.7 m, and depth of 1.2 m) in which all of the active elements are installed: the wall of aerogel tiles, the mirrors, the photomultiplier tubes (PMTs), and the electronics. The main structural elements of the box are: the two lateral panels made of aluminum sandwich, the top panel made of carbon-fiber sandwich, and the two upper angular elements and the bottom element made of aluminum. Each of the lateral

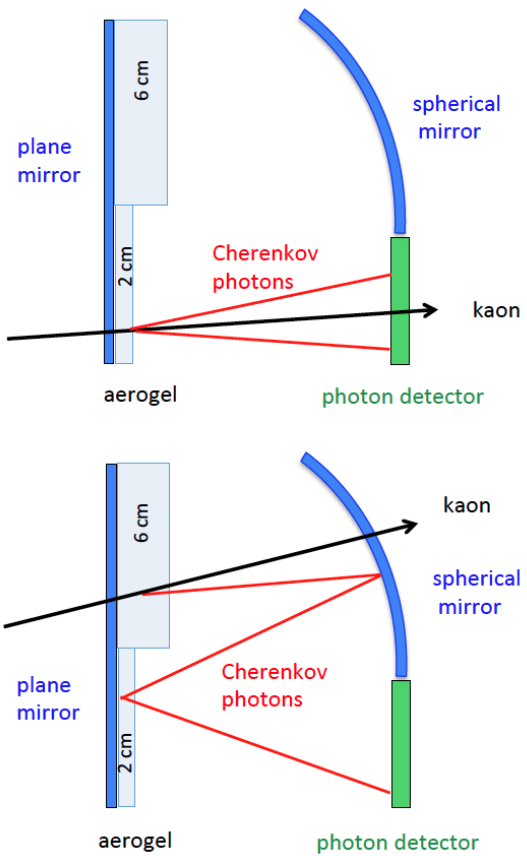


Figure 3: Examples of CLAS12 RICH imaging: direct detection of the Cherenkov cone produced in the thin aerogel layer (top plot); detection of the Cherenkov cone produced in the thick aerogel layer¹⁵³ after multiple reflections and passes through the thin aerogel layer¹⁵⁴ (bottom plot). The plot is not to scale.

¹¹³ panels supports two planar mirrors, while another planar
¹¹⁴ mirror is installed on the bottom of the box. The box
¹¹⁵ is closed on the front face (with respect to the beam
¹¹⁶ direction) by two entrance panels made of a sandwich
¹¹⁷ of two 1-mm-thick carbon-fiber skins glued on a Nomex
¹¹⁸ honeycomb core. Two planar mirrors with a wall of
¹¹⁹ 2-cm-thick aerogel tiles are installed on the lower entrance
¹²⁰ panel, while a wall made of two layers of 3-cm-thick aerogel
¹²¹ tiles is installed on the upper one. Therefore, the profile
¹²² of the entrance panels was specifically designed not only
¹²³ to ensure the best light and gas tightness, but also to
¹²⁴ include stiffening ribs for the installation of the mirrors
¹²⁵ and the aerogel. The same sandwich structure was used
¹²⁶ for the electronics panel, located on the bottom part of
¹²⁷ the backward face of the box. It is composed of a main
¹²⁸ panel where all of the front-end electronics and the PMTs
¹²⁹ are installed, and a thin cover. The panel and the cover
¹³⁰ are screwed together on the mechanical structure, making
¹³¹ a very rigid system. Finally, a very light exit panel made
¹³² of a thin Tedlar sheet glued on an aluminum frame not
¹³³ supporting any active element, closes the back face of the
¹³⁴ trapezoidal box.

¹³⁵ The total material budget of the detector is largely
¹³⁶ dominated by the electronics panel, which contributes to
¹³⁷ approximately $0.3X_0$ in the region from the beamline up
¹³⁸ to about 17° . A sizable contribution comes also from the
¹³⁹ aerogel (with a maximum contribution of $0.05X_0$ in the
¹⁴⁰ polar angles from 17° to 26°), while other active compo-
¹⁴¹ nents like the spherical and planar mirrors contribute only
¹⁴² $\approx 0.01X_0$ each. The total material budget of the passive
¹⁴³ elements is estimated to be, on average, below $0.05X_0$.

¹⁴⁴ The mechanical structures and all of the active elements
¹⁴⁵ (mirrors, aerogel, electronics, MaPMTs) define the RICH
¹⁴⁶ detector. The RICH is attached to the CLAS12 Forward
¹⁴⁷ Carriage by means of steel connections, attached to the
¹⁴⁸ angular and bottom elements. Detailed Finite Element
¹⁴⁹ Analysis (FEA) studies were performed in order to
¹⁵⁰ optimize the design of the detector with respect to the
¹⁵¹ maximum deformation allowed by the required accuracy of
¹⁵² the optical systems. These studies included optimization
¹⁵³ of the ratio between the skin and honeycomb thicknesses
¹⁵⁴ of the sandwich, and of the total thickness and profile of
¹⁵⁵ various stiffening and connection elements. Simulations of
¹⁵⁶ the load conditions during the assembly and installation
¹⁵⁷ of the detector and in the RICH final position in CLAS12
¹⁵⁸ were also performed together with a seismic analysis¹.
¹⁵⁹ These simulations demonstrated that all stresses produced
¹⁶⁰ on the detector elements during the installation are well
¹⁶¹ inside the elastic regime, and that the total deformations
¹⁶² expected when the RICH is installed in CLAS12 never
¹⁶³ exceed a few mm.

¹According to US regulations, seismic analyses are performed by increasing the expected weight load by 10%.

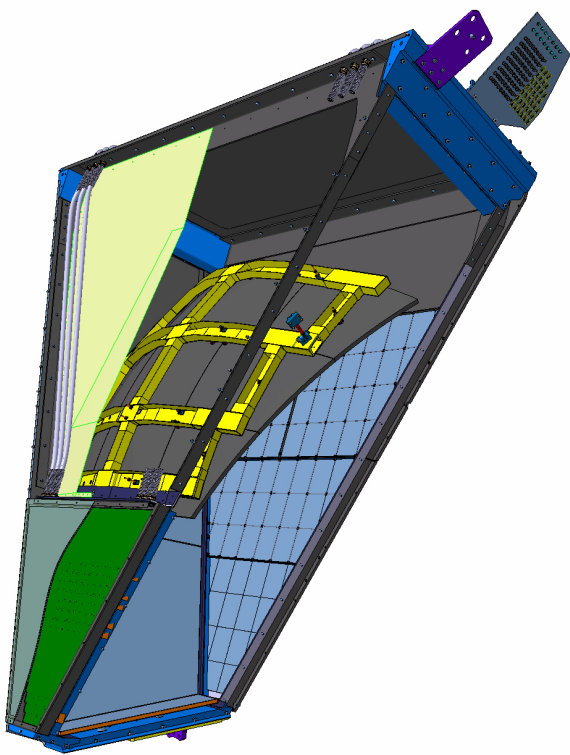


Figure 4: A schematic drawing of the CLAS12 RICH with the¹⁹⁹ internal components highlighted. From left to right, the components²⁰⁰ of the upper half are exit panel, spherical mirror support and²⁰¹ sub-mirrors, double 3-cm-thick aerogel layer, and entrance panel.²⁰² The components of the lower half are cover, electronics panel²⁰³ mounting the front-end readout and the MaPMT sensors, 2-cm-thick²⁰⁴ aerogel layer, front planar mirrors, and entrance panel.²⁰⁵

¹⁶⁴ 3. The RICH Detector Components

¹⁶⁵ 3.1. The Aerogel Radiator

¹⁶⁶ The aerogel radiator was produced by the *Budker and*
¹⁶⁷ *Boreskov Institute of Nuclear Physics* (Russia), which was
¹⁶⁸ able to fabricate tiles of different shapes and thicknesses,
¹⁶⁹ a critical requirement of the complex CLAS12 geometry.
¹⁷⁰ A total of 102 tiles with nominal refractive index 1.05,
¹⁷¹ cut into squares $200 \times 200 \text{ mm}^2$, as well as pentagonal,
¹⁷² trapezoidal, and triangular shapes, were assembled in two
¹⁷³ sections. The first section, covering the region between
¹⁷⁴ the beam pipe and the polar angle of 17.5° , was made of
¹⁷⁵ one layer of 2-cm-thick tiles. The second section, covering
¹⁷⁶ the polar angles between 17.5° and 26° , was made of two
¹⁷⁷ layers of 3-cm-thick tiles, the thickest aerogel tiles ever
¹⁷⁸ used in Cherenkov radiation applications at this high value
¹⁷⁹ of refractive index.

¹⁸⁰ Each tile was tested to determine the geometric and opti-
¹⁸¹ cal parameters [7]. The measured geometric parameters
¹⁸² are the side length and thickness, and the planarity of
¹⁸³ the tile surface. The measured optical parameters include
¹⁸⁴ the refractive index at the reference wavelength of 400 nm,
¹⁸⁵ and the light transmission as a function of the wavelength.
¹⁸⁶ The transparency parameter A_0 , the clarity parameter
¹⁸⁷ C , and the scattering length L_{scatt} at 400 nm are then
¹⁸⁸ extracted from the measured optical parameters using the
¹⁸⁹ Hunt parameterization [8]. Distributions of the measured
¹⁹⁰ values of the refractive index, A_0 (in percent), and L_{scatt}
¹⁹¹ for the square 2 cm tiles are shown in Fig. 5. The average
¹⁹² values obtained over all of the tiles are $L_{scatt} = 50.5 \text{ mm}$,
¹⁹³ $A_0 = 0.975$, and $C = 0.00512 \mu\text{m}^4/\text{cm}$. From these
¹⁹⁴ measurements, the expected photon yield for $\beta = 1$
¹⁹⁵ particles is estimated to be about 19 photoelectrons (p.e.)
¹⁹⁶ in the 2 cm sector and about 25 in the 6 cm (3 cm + 3 cm)
¹⁹⁷ sector.

¹⁹⁸ 3.2. The Mirror System

¹⁹⁹ The mirror system, composed of planar and spherical
²⁰⁰ mirrors, was designed to minimize the photon loss and
²⁰¹ to direct as much of the Cherenkov radiation as possible
²⁰² toward the photodetectors. Simulations were performed to
²⁰³ optimize the segmentation, the position, and the radius of
²⁰⁴ curvature of these mirrors, and to define the specifications
²⁰⁵ of the optical performance. A drawing of the system is
²⁰⁶ shown in Fig. 6.

²⁰⁷ 3.2.1. The Spherical Mirrors

²⁰⁸ The spherical mirror system, installed inside the box in
²⁰⁹ front of the exit panel, has a total surface of about 3.6 m^2 ,
²¹⁰ a radius of curvature $R = 2.7 \text{ m}$, and is segmented into
²¹¹ 10 sub-mirrors. They were produced by the *Composite*
²¹² *Mirror Applications* company [9], and are made of two
²¹³ layers of carbon fiber glued on a honeycomb core of small
²¹⁴ carbon-fiber cylinders. The areal weight of these mirrors
²¹⁵ is $\approx 5 \text{ kg/m}^2$, with an improvement of about 10% with
²¹⁶ respect to the mirrors produced by the same company

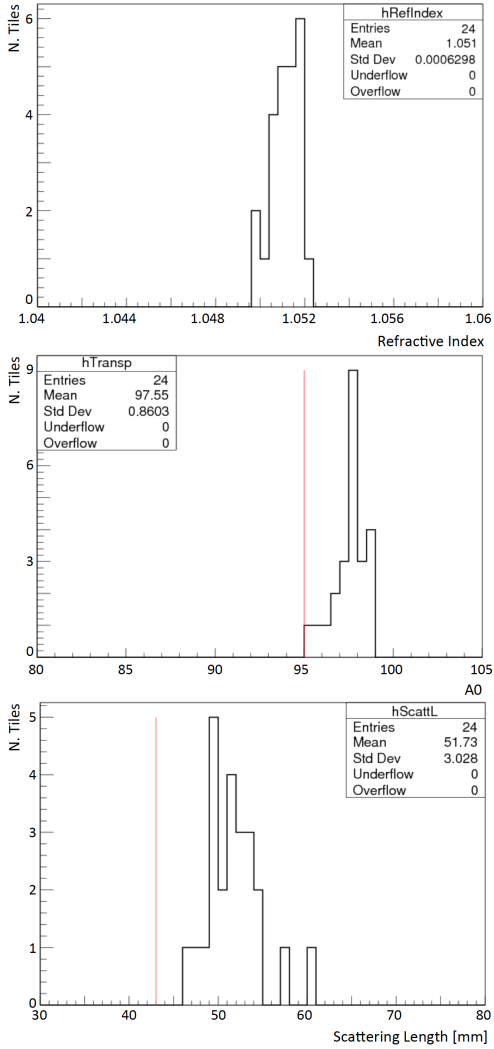


Figure 5: Distributions of the measured refractive index (top plot), A_0 (in percent, central plot), and L_{scatt} (bottom plot) for the square 2 cm tiles. The red lines indicate the specification limits.

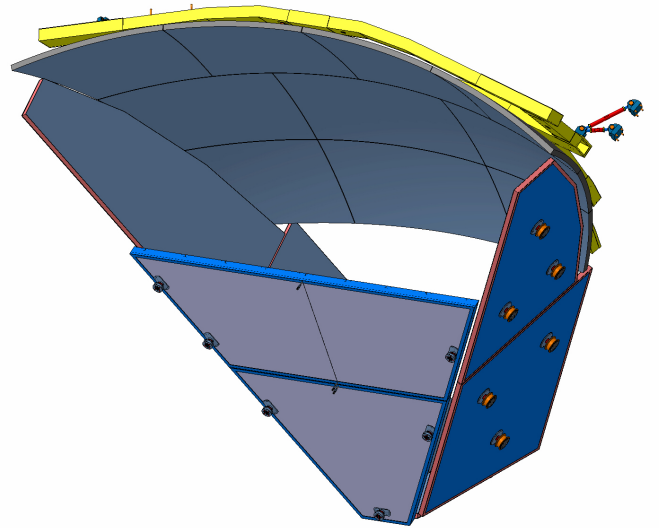


Figure 6: Drawing of the CLAS12 RICH mirror system with their mounting joints. The 10 sub-mirrors of the spherical mirror face the two front planar mirrors. An array of planar mirrors, two on each side and one (not visible) on the bottom, completes the light-containment system.

for the LHCb experiment [10]. Each mirror is positioned on a light carbon frame by means of three special joints equipped with a spring and a precision screw that allowed their relative alignment. The frame is then attached to the mechanical structure by means of three similar joints that allow the alignment of the full mirror system with respect to the other active elements of the detector.

The accuracy of the spherical surface of the sub-mirrors was quantified by means of a so-called spot size measurement, in which each mirror was illuminated with a point-like light source and the size of the reflected spot was measured by a XIMEA camera with a 1-cm-wide CMOS sensor. The size of the spot is quantified by D_0 , which is defined as the minimum diameter containing 90% of the total reflected light, and is related to the angular resolution of the reflected photons by the relation

$$\sigma_\theta = \frac{D_0}{8R}. \quad (1)$$

The smaller D_0 is, the closer the mirror surface is to a perfect sphere. The measurements also allow for the extraction of the radius of curvature, which corresponds to the distance between the camera and the mirror where the spot size is minimal. The results of a typical measurement of one sub-mirror are shown in Fig. 7, where D_0 as a function of the distance and the shape of the spot at the beginning of the distance scan and at the minimum are shown. All of the sub-mirrors exhibit a D_0 smaller than 1.5 mm, which means σ_θ significantly below 1 mrad, and a variation in the measured radii below 0.5%. All of these numbers are well within the specifications.

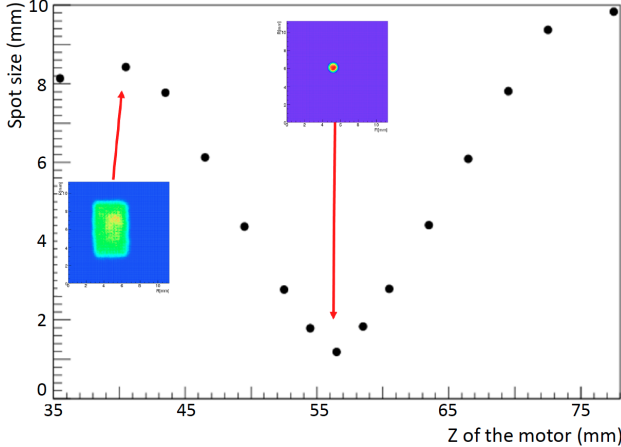


Figure 7: D_0 as function of the distance between the mirror and the camera for one of the spherical sub-mirrors. The two inserts show the shape of the reflected spot at the beginning of the distance scan and at the minimum.

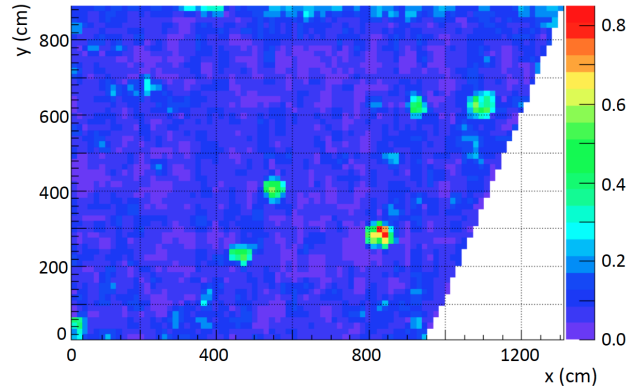


Figure 8: Profile of the local slope (indicated by the color scale in mrad) of the surface of one of the lateral planar mirror measured with a CMM.

245 The sub-mirrors were coated with a reflecting layer by
 246 *Evaporated Coatings Inc* [11]. The quality of this coating
 247 was verified by measuring the reflectivity on several surface²⁸³
 248 spots in the wavelength range from 300 to 650 nm. For all²⁸⁴
 249 of the sub-mirrors, we obtained on average a reflectivity²⁸⁵
 250 between 88% and 90%, relatively flat over the whole²⁸⁶
 251 wavelength range.²⁸⁷

252 3.2.2. The Planar Mirrors

253 The planar mirror system is composed of 7 mirrors: two²⁹⁰
 254 installed on each of the lateral panels, two on the front
 255 panel, and one on the bottom, for a total surface area of²⁹¹
 256 about 6.5 m². These mirrors were produced by the *Media₂₉₂*
 257 *Lario* company [12] and are made of two thin layers of glass²⁹³
 258 glued on an aluminum honeycomb core. This is a standard²⁹⁴
 259 technique widely used in telescopes for astrophysics studies²⁹⁵
 260 but used for the first time in nuclear physics experiments,²⁹⁶
 261 and allows for the production of mirrors as light as the²⁹⁷
 262 carbon fiber ones but at much lower cost. Being in the²⁹⁸
 263 acceptance of the detector, the front mirrors use very thin²⁹⁹
 264 (0.7 mm) glass layers, allowing a reduction of the material³⁰⁰
 265 budget down to about $0.01X_0$, while for the lateral and the³⁰¹
 266 bottom mirrors, thicker (1.6 mm) glass layers were used.³⁰²

267 The planarity of the mirror was measured with a³⁰³
 268 Coordinate Measuring Machine (CMM). Typically, the³⁰⁴
 269 measured accuracy of the surface was a few microns RMS.³⁰⁵
 270 To better quantify the quality of the surface, the local slope³⁰⁶
 271 profile was reconstructed from the spatial profile, as shown³⁰⁷
 272 for one of the lateral mirrors in Fig. 8, where we see only³⁰⁸
 273 a few spots with non-zero slope over a largely flat surface.³⁰⁹
 274 All of the mirrors satisfy the requirement that only a few³¹⁰
 275 percent of the total surface should exceed a local slope of³¹¹
 0.3 mrad.³¹²

277 The characterization of the planar mirrors was com-³¹³
 278 pleted by measuring the reflectivity in a few random spots³¹⁴
 279 of the surface in the wavelength range from 300 to 650 nm.³¹⁵

280 The measurements showed a maximum reflectivity of
 281 approximately 95% at 400 nm and a reflectivity higher
 282 than 90% in the whole range.

283 3.3. The Photon Detector

284 Thanks to the use of mirrors, the active area is
 285 minimized to about 1 m². The instrumented area is
 286 optimized to cover the most effective region close to the
 287 beam pipe, which is where the density of particles per unit
 288 area is the highest, the particle momenta are to a large
 289 extent above the FTOF working range, and the hadron
 290 identification requires the best RICH performance.

291 3.3.1. The Photosensor

292 Due to the imaging aspects of the RICH, there are
 293 several requirements that the photon sensor has to fulfill:
 294 it has to efficiently detect single photoelectron (SPE) level
 295 signals, it must be sensitive in the visible light wavelengths
 296 (due to the aerogel radiator material), it must have the
 297 spatial resolution required to achieve the design angular
 298 resolution, and it has to provide an active area with
 299 minimal dead space. In addition, it has to be insensitive
 300 to the low torus fringe field where the RICH readout is
 301 located, which is estimated to be no more than 3.5 G, see
 302 Fig. 9. The Hamamatsu flat-panel H8500 Multi-Anode
 303 PhotoMultiplier Tube (MaPMT) [13] with an 8×8 array of
 304 6×6 mm² pixels over a compact active area of 5×5 cm² and
 305 with high packing fractions (89%), was initially selected as
 306 a good candidate. Despite not advertised as the optimal
 307 choice in the SPE regime, such MaPMTs showed adequate
 308 performance in several laboratory tests [14] and beam
 309 tests [15]. Just after the RICH construction startup, the
 310 novel Hamamatsu H12700 became available, with the same
 311 layout as the H8500, but an optimized dynode structure
 312 for single photon detection [16].

313 Of the 391 MaPMTs that the CLAS12 RICH employs,
 314 80 are of the H8500 type and the rest are of the
 315 H12700 type. This results in a total of 25024 individual

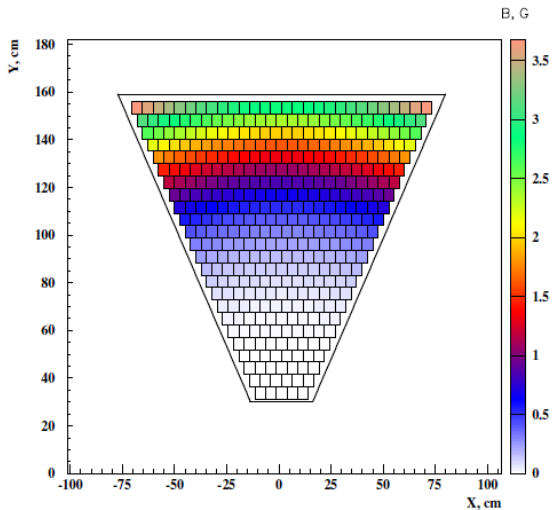


Figure 9: Calculated map of the torus fringe field strength (in Gauss) in the RICH photodetector area.

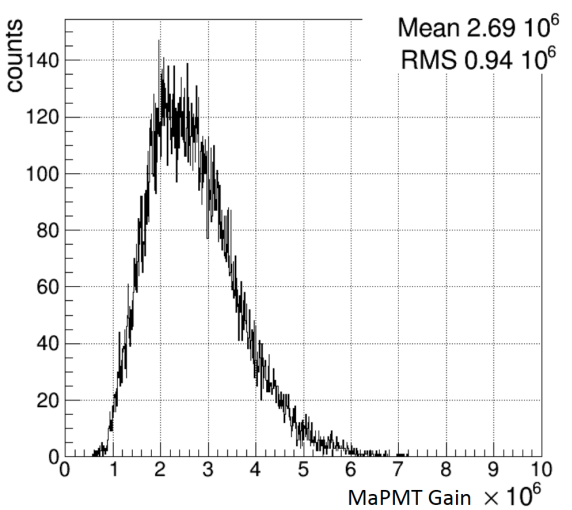


Figure 10: Distribution of the data-sheet gains of the 25k RICH MaPMT channels.

pixels, covering the $\sim 1 \text{ m}^2$ trapezoidal active area of the first RICH module. The production specifications included requirements on the minimum gain of 1×10^6 and a maximum total dark current of 5 nA. Both were fully achieved. Figure 10 shows the distribution of the pixel gains, which has an average value of 2.7×10^6 , corresponding to about 430 fC generated charge per SPE.

3.3.2. The Readout Electronics

The RICH front-end electronics are designed to ensure 100% efficiency at 1/3 of the average photoelectron signal level, 1 to 4 gain spread compensation, time resolution of the order of 1 ns to distinguish direct from reflected photon hits, and a trigger rate up to 20 kHz with 8 μs trigger latency and negligible dead time [17].

The front-end electronics are organized into compact units (called tiles, see Fig. 11) mechanically designed to fit the MaPMT dimensions, each serving two or three MaPMTs, thus allowing the tessellation of large surfaces with minimum dead space and material budget. Each readout unit comprises three boards with complementary functions.

A feed-through adapter board provides the electrical connectivity of the sensors with the external readout system, while preserving the adequate light and gas tightness of the inner detector volume when mounted on the RICH carbon-fiber supporting panel. It also distributes the sensor bias voltage (with -1000 V as the nominal value).

The signal processing board is based on the MAROC3 chip [18], a 64-channel microcircuit dedicated to MaPMT pulse processing. Each channel comprises a low impedance adjustable gain preamplifier followed by two highly configurable shaping sections with independent processing. The first section embeds a slow shaper and a sample-and-hold

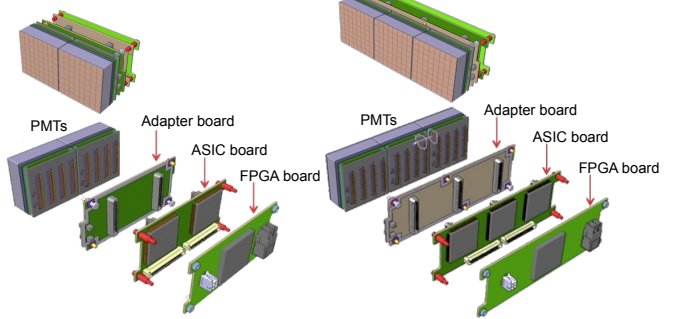


Figure 11: The CLAS12 RICH readout unit design (see text for details).

structure to allow linear charge measurements up to 5 pC. Requiring short trigger delays and multiplexed access, this section can be used as a RICH calibration tool. The second section features a fast shaper and an adjustable threshold discriminator to produce, for each input signal, a start and stop logic pulse. A constant-threshold binary readout requires good stability of the baseline (pedestal) and definition of the working point (gain and threshold). During the board production, quality assurance tests confirmed the excellent sensitivity of the logic readout, able to discriminate signals down to a few percent of a single photoelectron discharge, as will be extensively discussed in Section 4.2.

The third stage of the readout is made of the FPGA boards, hosting a Xilinx7 FPGA chip, responsible for configuring and reading the front-end MAROC3, distributing the trigger, and interfacing with the data acquisition system [19] via optical link. The FPGA provides a TDC functionality with a 1 ns time stamp for both start and stop times. The start time is used for timing purposes, while the difference between the stop and start

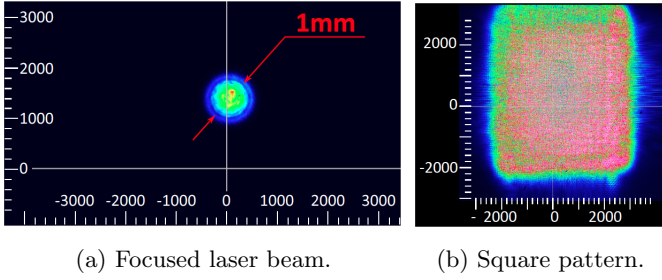


Figure 12: The MaPMT test stand laser output options.

times, the so-called Time-Over-Threshold (ToT), provides a non-linear estimate of the amplitude of the input signal and is used for the time-walk correction, see Section 5.2. Finally, the FPGAs also embed a scaler readout that is used as a calibration and monitoring tool.

3.3.3. MaPMT Characterization

The characterization of hundreds of MaPMTs is a challenging problem. In order to test them efficiently within a reasonable time frame, a fully automated test stand was built to evaluate 6 MaPMTs at once. The test stand consists of a 470 nm diode laser system, 2 long-travel motorized stands to drive a laser fiber in two-dimensional space for individual pixel illumination, and a motorized neutral-density filter system. The laser light is directed through the fiber and attenuated to the single-photon level using neutral-density filters to mimic the conditions of the RICH detector. The motors are remotely controlled to move the focused laser 1 mm beam spot across the entire surface of the MaPMT entrance window and illuminate one by one the 64 pixels individually (see Fig. 12a). Alternatively, one can illuminate the whole surface of the MaPMT photocathode at once using an Engineered Diffuser to produce a square pattern with a non-Gaussian intensity distribution (see Fig. 12b). The latter configuration was used for the massive characterization of the RICH MaPMTs, bringing routine workloads to a minimum. The evaluation of 6 MaPMTs (corresponding to 384 individual channels) at 4 different high voltages and 6 different light intensities was completed in 6 hours with less than 15 minutes of human intervention.

The characteristics of the SPE spectrum were studied using the charge measurement functionality of the slow shaper of the MAROC3 chip. A new computational model [20] for the description of the PMT response functions of both the H8500 and H12700 MaPMTs was developed. Important features of the model include the ability to approximate the true SPE spectra from different PMTs with a variety of parameterized spectral shapes. The predictive power of the model was tested by demonstrating that the SPE spectral parameters, obtained in the measurements, well describe the amplitude distributions of the same photodetector measured at different levels of illumination. Thus, the model allowed us to extract the

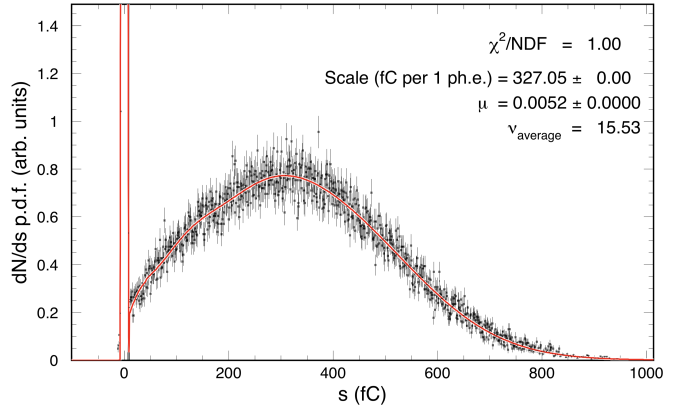


Figure 13: Sampled H8500 MaPMT single photoelectron spectrum from one of the pixels at 1000 V with a low-intensity laser light source. The fit function (see details in Ref. [20]) is shown as a solid line. The relevant parameters (see text) are $\mu = 0.0052$, $\nu_{\text{average}} = 15.53$, and $\text{scale} = 327 \text{ fC}$. This corresponds to a PMT gain of 2.0×10^6 .

characteristic parameters of the devices independently of the test measurement conditions.

The SPE spectrum is extracted by fitting the signal amplitude distribution with the model function measured as shown in Fig. 13 for the H8500 MaPMT and in Fig. 14 for the H12700. The x -axis is calibrated in terms of charge measured by the MAROC3 chip. To approximate the performance of the first amplification cascade of the MaPMTs, the probability function was introduced in the model as a trinomial sum of three Poissonians with different average secondary multiplicities and the corresponding three relative probabilities for every photoelectron to generate secondary electrons (see Ref. [20] for more details). In each fit, the parameter μ corresponds to the average number of photoelectrons generated at the photocathode by each laser pulse, ν_{average} is the average number of secondary electrons generated at the first dynode, and scale is the average anode charge collected from one photoelectron.

In the single-photoelectron amplitude spectra shown in Figs. 13 and 14, the normally significant contributions of the cross-talk signals caused by the photoelectron amplification cascades in the neighboring PMT channels, have been removed by using the filter masks covering the neighbors, and leaving open only the pixel studied. The detailed discussion of the method will be given in [21]. The data showed that the H12700 has, on average, a 10% better efficiency than the H8500, likely due to the improved photocathode performance and collection efficiency. An example of the results for one MaPMT is shown in Fig. 15. The parameter scale (top plot), characterizing the amplification (dynode) system, is virtually independent of the light radiation level, while strongly dependent on the high voltage setting, the exact behavior one would expect from the characteristics of the internal dynode system of a MaPMT. The central plot shows the average number

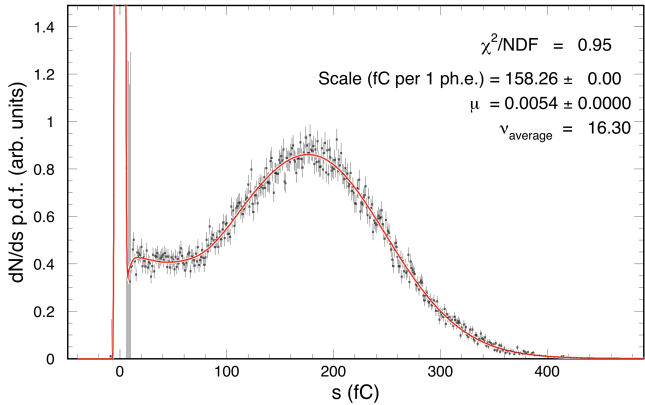


Figure 14: Sampled H12700 MaPMT single photoelectron spectrum from one of the pixels at 1000 V with a low-intensity laser light source. The fit function (see details in Ref. [20]) is shown as a solid line. The relevant parameters (see text) are $\mu = 0.0054$, $\nu_{\text{average}} = 16.3$, and $\text{scale} = 158.26$ fC. This corresponds to a PMT gain of 1.5×10^6 .

of photoelectrons μ measured with different optical filters. It indicates that all of the channels respond in the same way as the light intensity increases. This parameter is practically independent of the applied voltage, as expected. The parameter ν_{average} (bottom plot) that is related to the first dynode performance, has a weak dependence on the bias voltage and is independent of the level of light radiation as well.

The results of the characterization have been stored in the CLAS calibration database and are available for use in the Monte Carlo simulations. The extracted gain values have been used to perform the equalization of all 25024 readout channels.

The dark count spectra allow for the study of the SPE response dependence on the working parameters, i.e. MaPMT bias voltage, MAROC pre-amplification gain, and discriminator threshold ² using the binary readout line. Data indicated that the efficiency reaches a plateau over a wide range of working parameter values [17]. The plateau corresponds to the region where all of the MaPMT discharges are digitized and the efficiency ultimately depends on the quality of the photocathode. The plateau is a consequence of the saturated

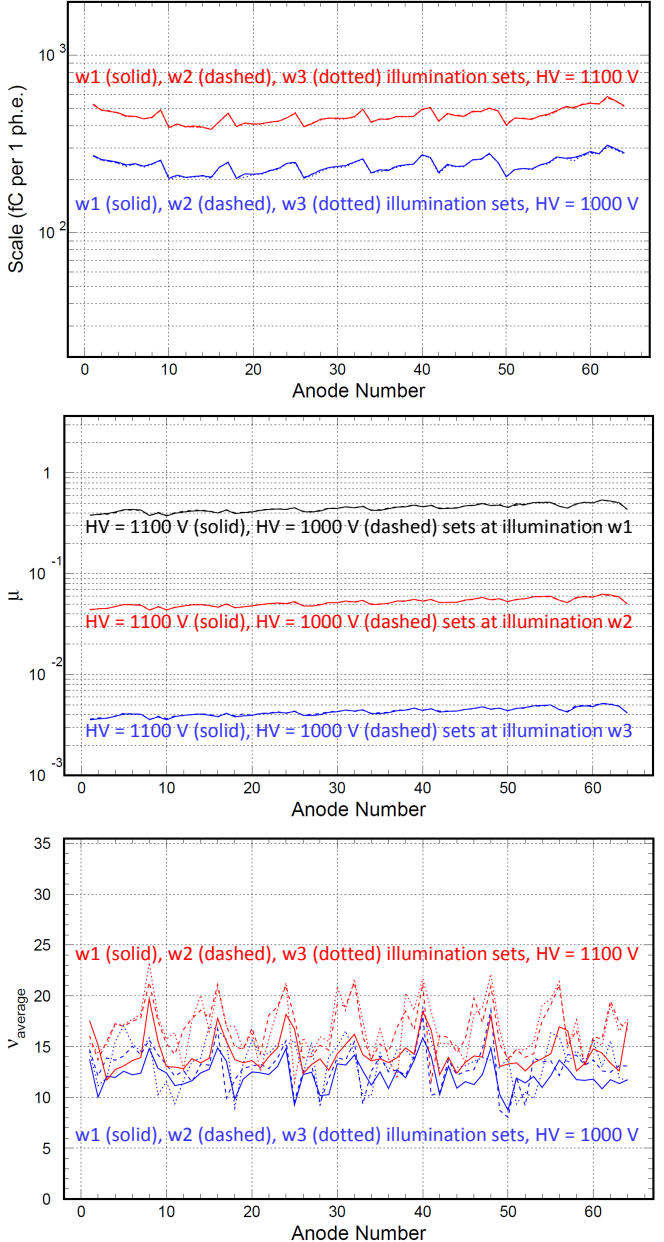


Figure 15: Distributions of fit parameters measured at 2 different high voltages (1000 V and 1100 V) and 3 different light intensities ($w_1:w_2:w_3 \sim 100:10:1$) for 64 pixels of one MaPMT: the parameter *scale* characterizing the dynode amplification system (top), the average number of photoelectrons μ (center), and the first dynode amplification ν (bottom).

²The programmed threshold levels are expressed in Digital-to-Analog Converter (DAC) units, 1 DAC unit corresponds to about 1 mV.

473 mode employed in the MAROC binary readout and allows
 474 a flexible definition of the working point, a crucial feature
 475 when dealing with a large number of channels in the
 476 challenging single-photon regime.

477 3.4. The Detector Services

478 The CLAS12 RICH requires various services, namely
 479 power, cooling, and gas purge whose number of lines has
 480 to be minimized and installed outside of the CLAS12
 481 acceptance. A continuous nitrogen flow, supplied by the
 482 Hall B gas distribution system, is provided in order to keep
 483 the relative humidity inside the RICH vessel at the few
 484 percent level. The flow is set to about 40 l/m to ensure
 485 a complete inner volume exchange every few hours. A
 486 backup system has been realized by a stack of nitrogen
 487 bottles to allow for up to 3 days of gas flow in case of
 488 failure of the primary distribution system.

489 The electronics power is controlled by a CAEN SY4527
 490 power supply with five 8-channel A2518 low voltage (LV)
 491 boards and five 32-channel A1536 high voltage (HV)
 492 boards. Each LV channel powers 4 readout units, while
 493 each HV channel drives the MaPMTs grouped in one
 494 readout unit. The electronics readout is connected to the
 495 back-end by three MTP trunks of 2.5 Gbps optical fibers.
 496 One trunk groups several multi-core fibers, each of them
 497 connecting one of the eight ports in the VME/SSP [19]
 498 back-end module to four FPGA boards.

499 The readout electronics dissipates about 3.5 W per unit,
 500 mainly due to the FPGA chip and the optical transceiver,
 501 as shown by the thermocamera image in Fig. 16. The
 502 total heat load, at the level of 500 W, is removed by a
 503 forced air flow. Since the electronics panel is not fully
 504 sealed due to the numerous holes for the readout and HV
 505 connectors, there is a diffusive exchange in the RICH vessel
 506 between the nitrogen gas used to keep the aerogel dry
 507 and the air in the electronics panel. As a consequence,
 508 dry and clean air is required to cool down the electronics.
 509 This is achieved with an Altas Copco multi-core oil-free
 510 rotary scroll air compressor. The compressor fills a tank
 511 at 8 atm pressure, from where the cooling air is filtered and
 512 circulated toward two distributors located at the sides of
 513 the electronics panel and outside the acceptance. These
 514 are made of stainless-steel tubes with several nozzles to
 515 direct the cooling air supersonic flow along the board
 516 surface. The exhaust is made of six corrugated tubes that
 517 run in the back of the RICH module behind the spherical
 518 mirror.

519 4. The RICH Detector Installation and Commis- 520 sioning

521 4.1. RICH Assembly

522 The assembly of the RICH detector was performed in
 523 a clean room and each element was installed after the
 524 completion of the relative characterization tests. The
 525 trapezoidal RICH vessel was attached to a large aluminum

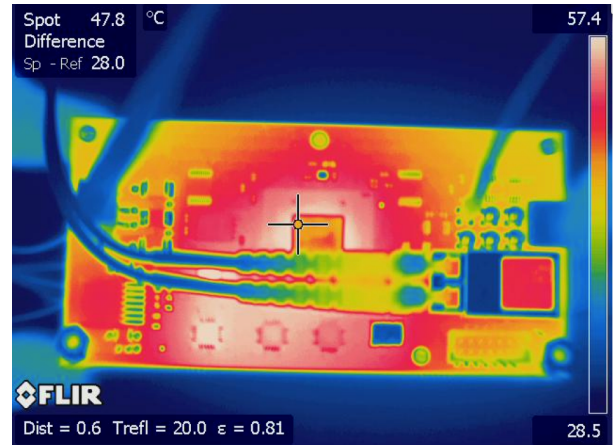


Figure 16: The CLAS12 RICH readout unit as imaged by a thermocamera. The hottest spots are the FPGA chip in the center and the optical transceiver on the right.

structure with a pivot to rotate the detector from the vertical to the horizontal position, as required by the various assembly phases.

The ten spherical sub-mirrors were mounted on a common frame inside the RICH vessel. To minimize the material budget, the frame is composed by a net of 1.5-mm-thick carbon-fiber U-profiles. Each element (frame and sub-mirrors) has three mounting points designed to allow precise alignment. The relative alignment of the sub-mirrors was performed with the same setup used to determine their surface accuracy. The full spherical mirror was illuminated by a point-like source and the position of each sub-mirror was adjusted until the ten spot images converged into the nominal center of curvature. In Fig. 17, the reflected images before the alignment (when each sub-mirror produces a spot at a different location) and after the alignment (when all the spots overlap within a few mm) are shown. The quality of the result is also visible in Fig. 18, where the spherical mirror system before (left) and after (right) the alignment is shown.

The lateral and bottom planar mirrors were attached to the RICH trapezoidal vessel structure by means of joints that allow for a precise alignment. The two front mirrors were mounted on the lower front panel made of carbon fiber. The relative position of the mirrors was aligned with respect to the RICH vessel at the level of about 0.5 mrad by using a faro-arm. The fully installed mirror system as seen from the entrance panel is shown in Fig. 19.

The RICH photon detectors and readout electronics were installed on the electronics panel using an independent aluminum support structure to enable easy access and to allow rotations during the functionality tests. The PMTs with higher gain were placed closer to the beam pipe, where better detection performance is required. As the MaPMT in one readout unit share the same HV bias, they were selected to be of similar gain and of the same type (H8500 or H12700). The fully equipped electronics

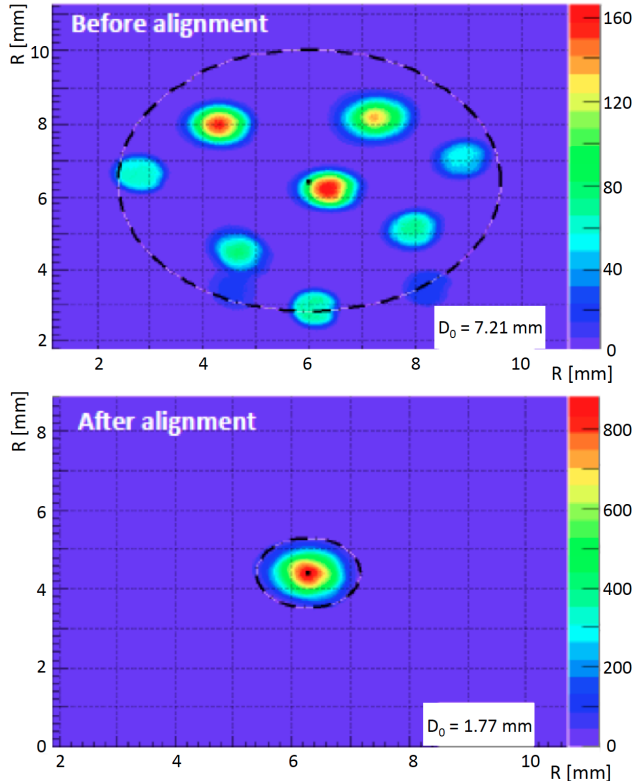


Figure 17: Reflected spot by the whole spherical mirror system: before the alignment (top plot), all sub-mirrors image the light source in different locations; after the alignment (bottom plot), all images overlap in the same position. The spot brightness depends on how close the sub-mirror center is to the sensor position.



Figure 18: The spherical mirror before (top plot) and after (bottom plot) alignment. As a result of the alignment, the image appears continuous along the whole mirror surface.

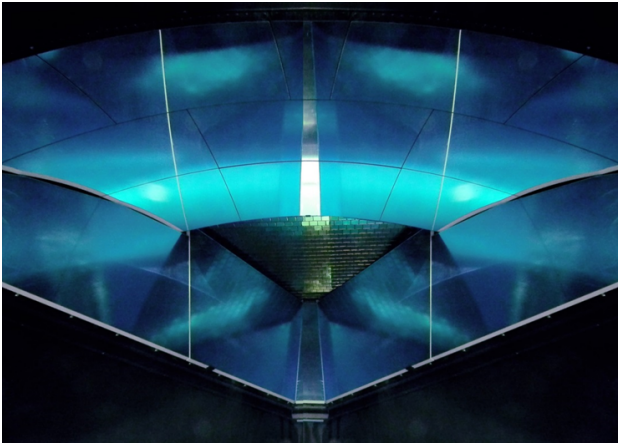


Figure 19: The mirror system as it is seen from the RICH entrance panel. Clockwise from the top, the ten spherical sub-mirrors, the two right lateral mirrors, the bottom mirror, and the two left lateral mirrors are visible. At the center, the MaPMT array is also visible.



Figure 20: The fully assembled plane of MaPMTs.

panel is shown in Fig. 20 from the MaPMT side and in Fig. 21 from the readout electronics side.

After the electronics panel assembly was completed, particular care was devoted to minimize and stabilize the pedestal width values. The measured pedestal RMS was initially at the level of few DAC units, with relatively large variations not only from MaPMT to MaPMT but also among the channels of a single MaPMT, as shown in the top plot of Fig. 22. As the readout uses a single threshold value per chip (or MaPMT), the channel-by-channel variation may effect the single channel efficiency in a way that would be complicated to correct for. Therefore, a grounding grid was realized by connecting all of the boards to the detector chassis with a copper wire. In this way, all of the components of the readout system, powered by floating 5 V low-voltage lines, were properly referred to the same ground. This reduced the typical pedestal RMS down to about 1 DAC unit, a level comparable with the test bench results, as shown in the bottom plot of Fig. 22.



Figure 21: The fully assembled and cabled front-end electronics. Visible are the gray 20 AWG LV cables, the red HTC-50-1-1 HV cables, and the cyan MTP optical fibers.

Several tests were performed using cosmic rays at various stages of the electronics assembly. In the absence of a precise measure of the cosmic particle momentum, it was not possible to perform any study of the Cherenkov angle resolution. Nevertheless, cosmic runs allowed for the validation of the translation tables relating the electronics channels to the pixel positions, the development of the ring reconstruction software, the verification of the stability of the system, and the testing of the performance of the power supplies, cooling, readout, slow controls, and interlock services. After all planned tests were completed, the complete readout system was eventually transferred into the mechanical structure.

The aerogel was the last element installed, being the most sensitive to the external conditions. For this reason, before its assembly, a test to verify the gas-tightness of the RICH vessel, temporarily completed with all of the closing panels, was performed. Each aerogel tile was inspected and mounted in a pre-selected location of the supporting structure, namely the front mirrors for the 2-cm tiles and the upper front panel for the 3-cm tiles. The location of each tile was determined in order to concentrate the tiles with the higher expected photon yield at forward polar angles where the particle identification requirements are most demanding. In addition, tiles with close optical properties were coupled in the same location of the double 3-cm layer. The tiles were secured in place by a net of nylon wires that ran along the edges and, on the side, by plastic bumpers covered by a thin foam layer to avoid damage to the aerogel. The tiles were also optically isolated from each other by using a thin layer of foam stretched around each tile. In fact, photons produced in one tile and propagating through an adjacent tile undergo surface effects that generally degrade the angular resolution. The foam is instrumental to avoid sharp edge contacts between the blocks that might originate cracks in the aerogel material. In addition, the foam net bonds the tiles together in forming a sole and stable layer. Figure 23 shows the front planar mirror system with the aerogel tiles fully installed.

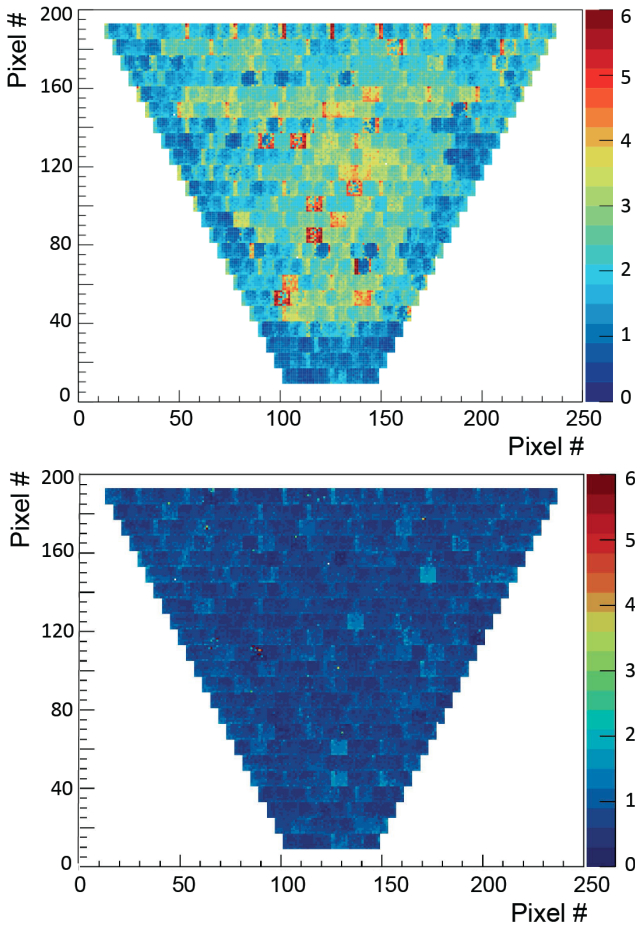


Figure 22: Map of the pedestal RMS values before (top) and after (bottom) the realization of a grounding grid connecting all of the electronics units to the RICH chassis to provide a common ground reference for the floating power lines.

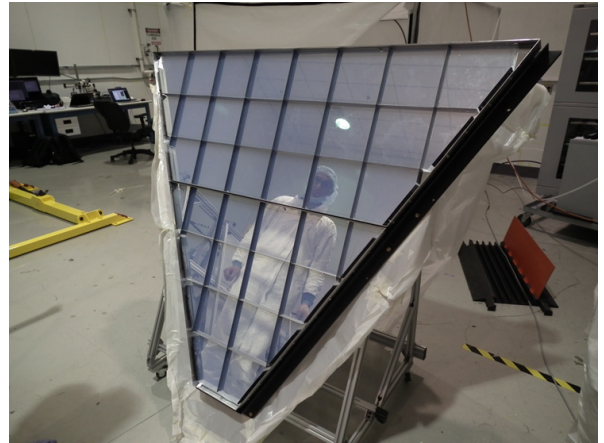


Figure 23: The 2-cm-thick section of the aerogel mounted on the two RICH front mirrors. Visible are the external aluminum frame and the black foam net that optically and mechanically isolates each tile from the others.

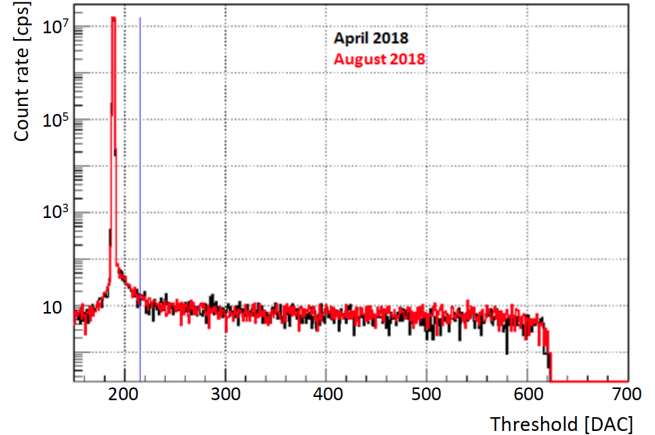


Figure 24: Example of a SPE spectrum from the dark rate measurement of one readout channel as a function of the threshold value. The two histograms were recorded in April and August 2018. The blue line indicates the threshold setting.

During the assembly, the aerogel panels were maintained in a low-humidity atmosphere (around 20% relative humidity) to prevent moisture absorption. Once the assembly of all tiles was completed, the panels were quickly installed on the RICH vessel, the detector was sealed with all of the closing panels and a flow of purged nitrogen was started to minimize the exposure to the external environment conditions.

Once the detector was sealed and before the transportation to the experimental hall, its functional parameters were tested for several weeks in the assembly room. The tests included the two gas systems serving the RICH: the nitrogen system that must keep the internal humidity at the few percent level to preserve the aerogel optical performance and the air-cooling system of the readout electronics.

4.2. RICH Commissioning

The RICH detector was installed in the CLAS12 spectrometer at the beginning of January 2018, in time with the start of the first data taking in Hall B. In preparation

for the data taking, a number of tests were routinely performed without and with beam to establish the running conditions and to verify the stability of the response.

The basic tool to monitor the RICH front-end electronics is provided by the measurement of the MaPMT dark noise counting rate. The number of counts above a programmed threshold is recorded for a time on the order of a second. A fine scan of the threshold value allows for the reconstruction of the full SPE spectrum for each of the 25k channels. An example of one SPE spectrum is shown in Fig. 24. The main features of the data are: *a)* a very narrow pedestal where the threshold equals the analog baseline, *b)* a region close to the pedestal where the rate smoothly decreases as the threshold increases (corresponding to the almost linear regime of the MAROC), and *c)* a large plateau of the saturation

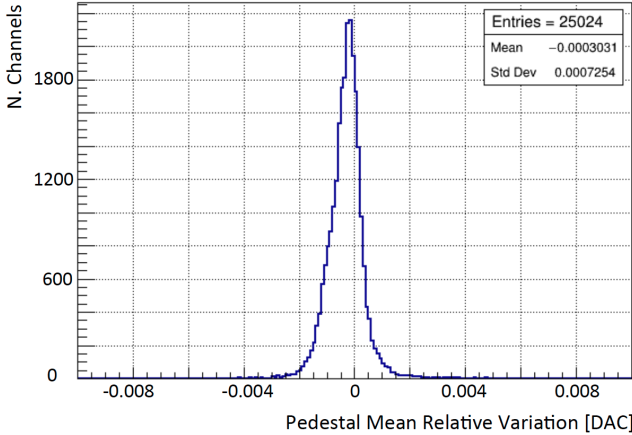


Figure 25: Relative variation of the mean pedestal position of the 25024 readout channels between April and August 2018.

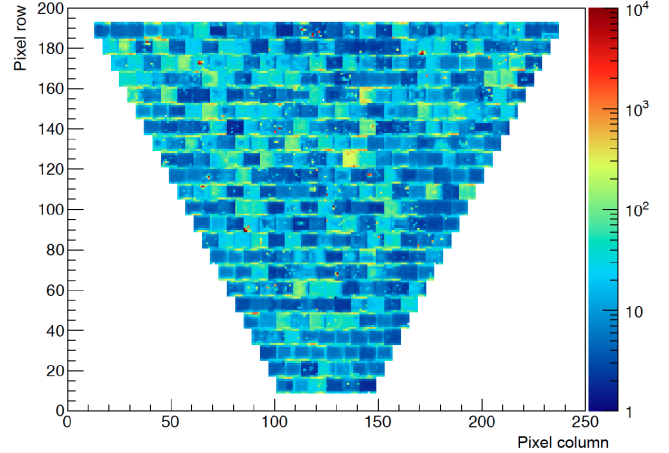


Figure 27: Map of the average dark count rate in the plateau region of threshold values (color scale).

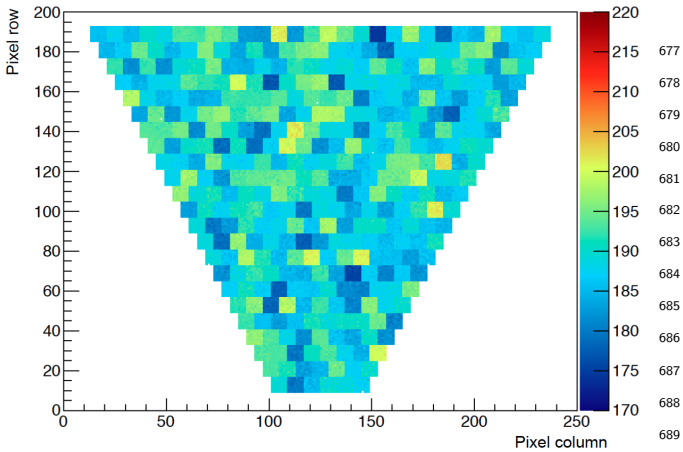


Figure 26: Map of the mean pedestal position in DAC units (color scale).

regime, where the count rate is basically insensitive to the threshold setting almost up to the edge of the SPE region. The plateau is a crucial feature of the front-end electronics, because it allows a flexible definition of the working point without the need for extreme precision in the channel equalization. The spectra allow for the channel-by-channel extraction of the pedestal position and width, the dark count rate in the plateau region, and the amplitude of the SPE region. The black and red histograms in Fig. 24, taken in April and August 2018, respectively, demonstrate the stability of the readout system over several months of running. Moreover, in Fig. 25, the relative variation of the mean pedestal position in the same interval of time is shown. On average, the pedestals are stable at the level of 10^{-3} .

The pedestal level is different for each readout channel, but it is quite uniform within one MAROC chip, as can be seen from the map shown in Fig. 26. This result guarantees the effectiveness of the common threshold.

The average count rate in the plateau region provides a measurement of the dark count rate of the channel, as shown in the map of Fig. 27. The typical dark count rate is a few tens of Hz, with more than 99% of the channels below 100 Hz and only few channels above 10 kHz. It is also found that the highest dark count rates in the MaPMTs are located in the first and last row of pixels. Although measured with a completely different setup, these results are in good agreement with the values quoted in the Hamamatsu data sheets.

The MAROC preamplifier equalization gains are determined using the characterization measurements described in Section 3.3.3 by tuning the average MaPMT+MAROC gain to 2.7×10^6 in all channels. The equalization gains range from about 0.5 to 3, with an average value of 1.2. The effect of the channel-by-channel signal equalization was verified during the engineering run by taking data at various thresholds for different MAROC gain configurations. Figure 28 shows the ToT distribution for three typical values of the threshold, on the top for all channels without amplification (nominal MAROC gain of 1) and on the bottom after equalization. After equalization, the ToT distribution of saturated SPE signals is narrower than with unitary gains. With typical ToT values larger than 40 ns, the signal region is also clearly separated from the cross-talk signals whose ToT values are distributed around 25 ns.

After these tests, the common discriminator thresholds were set to +25 DAC units above the average MaPMT pedestal position, a level that corresponds to a small fraction of the average SPE amplitude.

4.3. RICH Slow Controls and Interlocks

The RICH slow controls are based on Experimental Physics Industrial Control System (EPICS) [22]. It includes EPICS input-output controllers (IOCs) interfacing with different types of hardware via communication

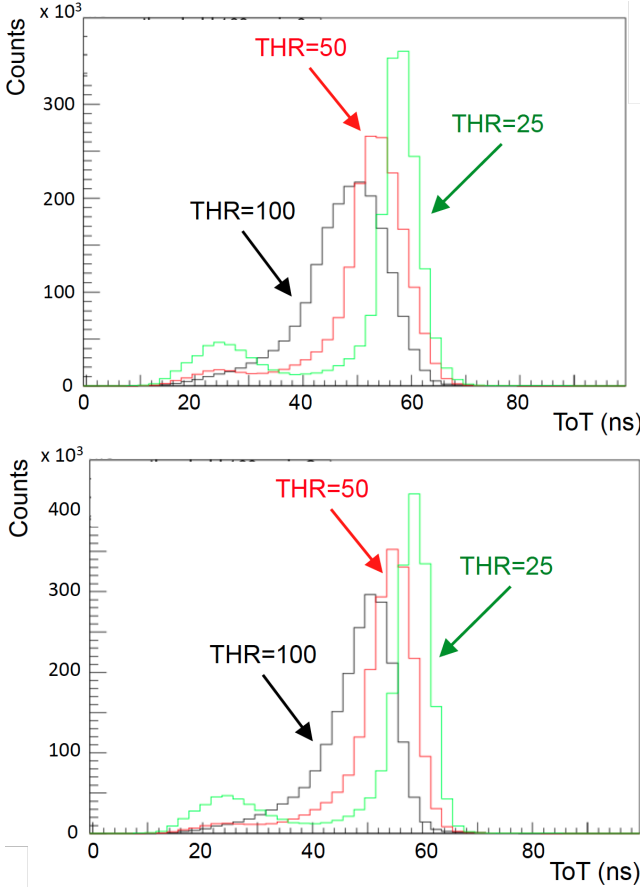


Figure 28: Time-over-Threshold (ToT) distributions of the RICH channels at three typical values of threshold (25, 50, and 100 DAC) without (top) and with (bottom) gain equalization. The saturated SPE signals generally yield ToT durations greater than 40 ns. When lowering the threshold weaker cross-talk signals are also recorded with ToT durations around 25 ns. Figure taken from Ref. [17].

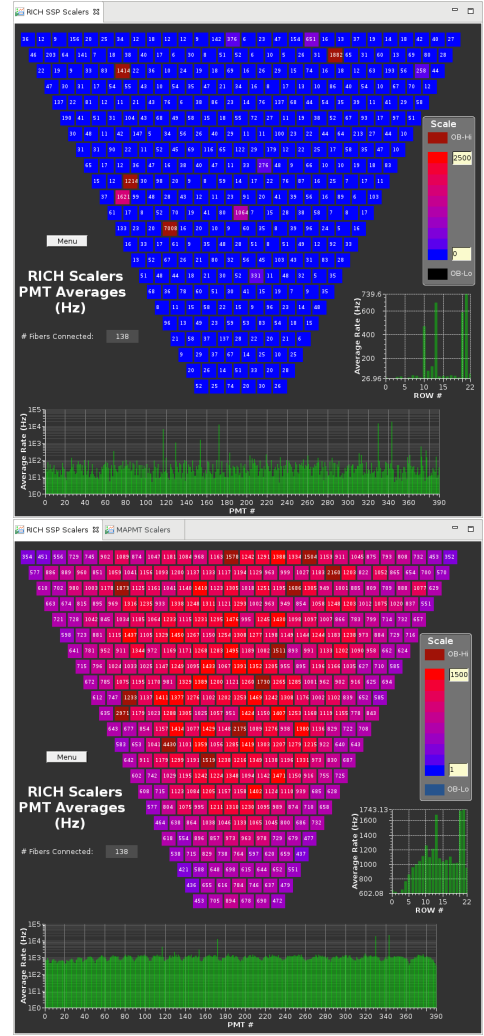


Figure 29: The average count rates (in Hz) over 64 pixels for each MaPMT during data taking. Top: without beam on target, Bottom: with beam.

713 protocols and over 25k RICH process variables (PVs).
 714 The controls system monitors many aspects of the RICH
 715 detector, such as the scaler rates of all 25k Hamamatsu
 716 MaPMT pixels, the FPGA temperatures of each readout
 717 board, the HV and LV power supplies, the LV and current
 718 consumption of each readout unit, the gas system, and
 719 the temperature and humidity of the electronics panel
 720 volume and detector volume. For the Graphical User In-
 721 terface (GUI), the Control Systems Studio (CS-Studio), an
 722 Eclipse-based suite of tools for developing and monitoring
 723 large-scale control systems, is used.
 742

The quality of the data is monitored by scaler and TDC
 725 plots. Figure 29 shows the average MaPMT rate measured
 726 by the scaler readout system when the beam is off (top)
 727 plot) and when the beam is on (bottom plot). In the top
 728 plot, the few MaPMTs with hot pixels where the dark
 729 rate is substantially higher than the average can easily be
 730 seen. The bottom plot shows that when the beam is on
 731 the rate is always dominated by physics events. Figure 30
 732 shows the occupancy plots from the TDC readout. The
 733 top plot shows the occupancy per channel, and the center

and bottom plots show the distributions of the leading
 734 and trailing edge times per MaPMT, respectively. All of
 735 these plots are used during the data taking to identify
 736 possible malfunctioning channels and, eventually, restore
 737 them through a recovery procedure.

The slow controls and monitoring of the RICH detector
 738 is enforced by the hardware interlock system based on
 739 the National Instruments CompactRIO (cRIO) [23]. The
 740 cRIO system monitors the following parameters:

- Temperature and humidity in 16 locations of the
 741 detector volume;
- Temperature and humidity in 16 locations of the
 742 electronics panel;
- Air tank pressure;
- Air and nitrogen flow.

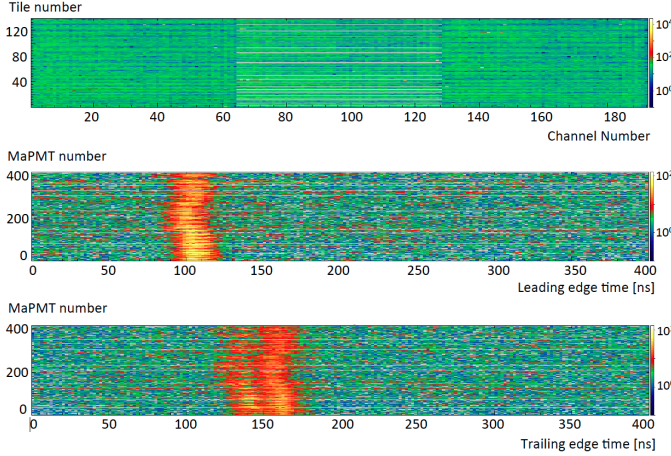


Figure 30: Online monitor plots of the TDC occupancy with beam on. From top to bottom: channel occupancy in terms of the tile vs. channel number; leading edge time distributions per MaPMT; trailing edge time distribution per MaPMT.

749 The locations of the temperature and humidity sensors,
 750 and the air and nitrogen flows fed into the electronics
 751 panel and nitrogen volume are shown in Figs. 31 and 32,
 752 respectively. The inner temperature of the electronics⁷⁵³
 753 panel ranges between 34.5°C and 44.5°C moving from⁷⁵⁴
 754 the bottom towards the top of the module, whereas the
 755 external temperature stays below 34.5°C, in accordance⁷⁵⁶
 756 with the requirement to not drive the FTOF system above
 757 40°C. The relative humidity is below 0.5%. In the nitrogen⁷⁵⁸
 758 volume, the temperature ranges between 23°C and 27°C.⁷⁵⁹
 759 The relative humidity is below 1.3% except in the central⁷⁶⁰
 760 point close to the spherical mirror pivot, where it reaches⁷⁶¹
 761 a 3% value. 792

762 The signal levels are controlled by setting limits. If the⁷⁶³
 763 temperatures, air flow, or air pressure go out of limits, the⁷⁶⁴
 764 HV and LV are powered off, i.e. interlocked. In case the⁷⁶⁵
 765 humidity or the nitrogen flow are out of limits, an alarm⁷⁶⁶
 766 signal is generated. 797

767 Important safety parameters of the RICH detector are:⁷⁶⁸
 768 the temperature of the front-end electronics, the nitrogen⁷⁶⁹
 769 flow, and the RICH internal relative humidity. Figure 33⁷⁷⁰
 770 presents the map of the temperatures of the front-end⁷⁸⁰
 780 electronics. Typical temperature values are around 65°C⁷⁸¹
 781 on the FPGA chips and 40°C in the detector volume. The⁷⁸²
 782 safety temperature limits are 85°C for the FPGAs, 80°C⁷⁸³
 783 for the optical fiber cables, and 40°C for the temperature⁷⁸⁴
 784 on the FTOF detector, which is about 10 cm away from⁷⁸⁵
 785 the RICH. Therefore, the maximum allowed temperature⁷⁸⁶
 786 was set to 75°C on the FPGA and to 45°C inside the⁷⁸⁷
 787 electronics panel. 809

789 The nitrogen flow and the RICH internal relative⁸⁰⁰
 800 humidity are measured by several probes installed inside⁸⁰¹
 801 the detector. An alarm is sent out in case the humidity⁸⁰²
 802 exceeds 5% or in case the nitrogen flow drops below the⁸⁰³
 803 normal value. In the latter case, the backup system starts⁸⁰⁴
 804 working to restore the normal flow level and to ensure⁸⁰⁵
 805 working to restore the normal flow level and to ensure⁸⁰⁶
 806 working to restore the normal flow level and to ensure⁸⁰⁷
 807 working to restore the normal flow level and to ensure⁸⁰⁸
 808 working to restore the normal flow level and to ensure⁸⁰⁹
 809 working to restore the normal flow level and to ensure⁸¹⁰
 810 working to restore the normal flow level and to ensure⁸¹¹
 811 working to restore the normal flow level and to ensure⁸¹²
 812 working to restore the normal flow level and to ensure⁸¹³
 813 working to restore the normal flow level and to ensure⁸¹⁴
 814 working to restore the normal flow level and to ensure⁸¹⁵
 815 working to restore the normal flow level and to ensure⁸¹⁶
 816 working to restore the normal flow level and to ensure⁸¹⁷
 817 working to restore the normal flow level and to ensure⁸¹⁸
 818 working to restore the normal flow level and to ensure⁸¹⁹
 819 working to restore the normal flow level and to ensure⁸²⁰
 820 working to restore the normal flow level and to ensure⁸²¹
 821 working to restore the normal flow level and to ensure⁸²²
 822 working to restore the normal flow level and to ensure⁸²³
 823 working to restore the normal flow level and to ensure⁸²⁴
 824 working to restore the normal flow level and to ensure⁸²⁵
 825 working to restore the normal flow level and to ensure⁸²⁶
 826 working to restore the normal flow level and to ensure⁸²⁷
 827 working to restore the normal flow level and to ensure⁸²⁸
 828 working to restore the normal flow level and to ensure⁸²⁹
 829 working to restore the normal flow level and to ensure⁸³⁰
 830 working to restore the normal flow level and to ensure⁸³¹
 831 working to restore the normal flow level and to ensure⁸³²
 832 working to restore the normal flow level and to ensure⁸³³
 833 working to restore the normal flow level and to ensure⁸³⁴
 834 working to restore the normal flow level and to ensure⁸³⁵
 835 working to restore the normal flow level and to ensure⁸³⁶
 836 working to restore the normal flow level and to ensure⁸³⁷
 837 working to restore the normal flow level and to ensure⁸³⁸
 838 working to restore the normal flow level and to ensure⁸³⁹
 839 working to restore the normal flow level and to ensure⁸⁴⁰
 840 working to restore the normal flow level and to ensure⁸⁴¹
 841 working to restore the normal flow level and to ensure⁸⁴²
 842 working to restore the normal flow level and to ensure⁸⁴³
 843 working to restore the normal flow level and to ensure⁸⁴⁴
 844 working to restore the normal flow level and to ensure⁸⁴⁵
 845 working to restore the normal flow level and to ensure⁸⁴⁶
 846 working to restore the normal flow level and to ensure⁸⁴⁷
 847 working to restore the normal flow level and to ensure⁸⁴⁸
 848 working to restore the normal flow level and to ensure⁸⁴⁹
 849 working to restore the normal flow level and to ensure⁸⁵⁰
 850 working to restore the normal flow level and to ensure⁸⁵¹
 851 working to restore the normal flow level and to ensure⁸⁵²
 852 working to restore the normal flow level and to ensure⁸⁵³
 853 working to restore the normal flow level and to ensure⁸⁵⁴
 854 working to restore the normal flow level and to ensure⁸⁵⁵
 855 working to restore the normal flow level and to ensure⁸⁵⁶
 856 working to restore the normal flow level and to ensure⁸⁵⁷
 857 working to restore the normal flow level and to ensure⁸⁵⁸
 858 working to restore the normal flow level and to ensure⁸⁵⁹
 859 working to restore the normal flow level and to ensure⁸⁶⁰
 860 working to restore the normal flow level and to ensure⁸⁶¹
 861 working to restore the normal flow level and to ensure⁸⁶²
 862 working to restore the normal flow level and to ensure⁸⁶³
 863 working to restore the normal flow level and to ensure⁸⁶⁴
 864 working to restore the normal flow level and to ensure⁸⁶⁵
 865 working to restore the normal flow level and to ensure⁸⁶⁶
 866 working to restore the normal flow level and to ensure⁸⁶⁷
 867 working to restore the normal flow level and to ensure⁸⁶⁸
 868 working to restore the normal flow level and to ensure⁸⁶⁹
 869 working to restore the normal flow level and to ensure⁸⁷⁰
 870 working to restore the normal flow level and to ensure⁸⁷¹
 871 working to restore the normal flow level and to ensure⁸⁷²
 872 working to restore the normal flow level and to ensure⁸⁷³
 873 working to restore the normal flow level and to ensure⁸⁷⁴
 874 working to restore the normal flow level and to ensure⁸⁷⁵
 875 working to restore the normal flow level and to ensure⁸⁷⁶
 876 working to restore the normal flow level and to ensure⁸⁷⁷
 877 working to restore the normal flow level and to ensure⁸⁷⁸
 878 working to restore the normal flow level and to ensure⁸⁷⁹
 879 working to restore the normal flow level and to ensure⁸⁸⁰
 880 working to restore the normal flow level and to ensure⁸⁸¹
 881 working to restore the normal flow level and to ensure⁸⁸²
 882 working to restore the normal flow level and to ensure⁸⁸³
 883 working to restore the normal flow level and to ensure⁸⁸⁴
 884 working to restore the normal flow level and to ensure⁸⁸⁵
 885 working to restore the normal flow level and to ensure⁸⁸⁶
 886 working to restore the normal flow level and to ensure⁸⁸⁷
 887 working to restore the normal flow level and to ensure⁸⁸⁸
 888 working to restore the normal flow level and to ensure⁸⁸⁹
 889 working to restore the normal flow level and to ensure⁸⁹⁰
 890 working to restore the normal flow level and to ensure⁸⁹¹
 891 working to restore the normal flow level and to ensure⁸⁹²
 892 working to restore the normal flow level and to ensure⁸⁹³
 893 working to restore the normal flow level and to ensure⁸⁹⁴
 894 working to restore the normal flow level and to ensure⁸⁹⁵
 895 working to restore the normal flow level and to ensure⁸⁹⁶
 896 working to restore the normal flow level and to ensure⁸⁹⁷
 897 working to restore the normal flow level and to ensure⁸⁹⁸
 898 working to restore the normal flow level and to ensure⁸⁹⁹
 899 working to restore the normal flow level and to ensure⁹⁰⁰
 900 working to restore the normal flow level and to ensure⁹⁰¹
 901 working to restore the normal flow level and to ensure⁹⁰²
 902 working to restore the normal flow level and to ensure⁹⁰³
 903 working to restore the normal flow level and to ensure⁹⁰⁴
 904 working to restore the normal flow level and to ensure⁹⁰⁵
 905 working to restore the normal flow level and to ensure⁹⁰⁶
 906 working to restore the normal flow level and to ensure⁹⁰⁷
 907 working to restore the normal flow level and to ensure⁹⁰⁸
 908 working to restore the normal flow level and to ensure⁹⁰⁹
 909 working to restore the normal flow level and to ensure⁹¹⁰
 910 working to restore the normal flow level and to ensure⁹¹¹
 911 working to restore the normal flow level and to ensure⁹¹²
 912 working to restore the normal flow level and to ensure⁹¹³
 913 working to restore the normal flow level and to ensure⁹¹⁴
 914 working to restore the normal flow level and to ensure⁹¹⁵
 915 working to restore the normal flow level and to ensure⁹¹⁶
 916 working to restore the normal flow level and to ensure⁹¹⁷
 917 working to restore the normal flow level and to ensure⁹¹⁸
 918 working to restore the normal flow level and to ensure⁹¹⁹
 919 working to restore the normal flow level and to ensure⁹²⁰
 920 working to restore the normal flow level and to ensure⁹²¹
 921 working to restore the normal flow level and to ensure⁹²²
 922 working to restore the normal flow level and to ensure⁹²³
 923 working to restore the normal flow level and to ensure⁹²⁴
 924 working to restore the normal flow level and to ensure⁹²⁵
 925 working to restore the normal flow level and to ensure⁹²⁶
 926 working to restore the normal flow level and to ensure⁹²⁷
 927 working to restore the normal flow level and to ensure⁹²⁸
 928 working to restore the normal flow level and to ensure⁹²⁹
 929 working to restore the normal flow level and to ensure⁹³⁰
 930 working to restore the normal flow level and to ensure⁹³¹
 931 working to restore the normal flow level and to ensure⁹³²
 932 working to restore the normal flow level and to ensure⁹³³
 933 working to restore the normal flow level and to ensure⁹³⁴
 934 working to restore the normal flow level and to ensure⁹³⁵
 935 working to restore the normal flow level and to ensure⁹³⁶
 936 working to restore the normal flow level and to ensure⁹³⁷
 937 working to restore the normal flow level and to ensure⁹³⁸
 938 working to restore the normal flow level and to ensure⁹³⁹
 939 working to restore the normal flow level and to ensure⁹⁴⁰
 940 working to restore the normal flow level and to ensure⁹⁴¹
 941 working to restore the normal flow level and to ensure⁹⁴²
 942 working to restore the normal flow level and to ensure⁹⁴³
 943 working to restore the normal flow level and to ensure⁹⁴⁴
 944 working to restore the normal flow level and to ensure⁹⁴⁵
 945 working to restore the normal flow level and to ensure⁹⁴⁶
 946 working to restore the normal flow level and to ensure⁹⁴⁷
 947 working to restore the normal flow level and to ensure⁹⁴⁸
 948 working to restore the normal flow level and to ensure⁹⁴⁹
 949 working to restore the normal flow level and to ensure⁹⁵⁰
 950 working to restore the normal flow level and to ensure⁹⁵¹
 951 working to restore the normal flow level and to ensure⁹⁵²
 952 working to restore the normal flow level and to ensure⁹⁵³
 953 working to restore the normal flow level and to ensure⁹⁵⁴
 954 working to restore the normal flow level and to ensure⁹⁵⁵
 955 working to restore the normal flow level and to ensure⁹⁵⁶
 956 working to restore the normal flow level and to ensure⁹⁵⁷
 957 working to restore the normal flow level and to ensure⁹⁵⁸
 958 working to restore the normal flow level and to ensure⁹⁵⁹
 959 working to restore the normal flow level and to ensure⁹⁶⁰
 960 working to restore the normal flow level and to ensure⁹⁶¹
 961 working to restore the normal flow level and to ensure⁹⁶²
 962 working to restore the normal flow level and to ensure⁹⁶³
 963 working to restore the normal flow level and to ensure⁹⁶⁴
 964 working to restore the normal flow level and to ensure⁹⁶⁵
 965 working to restore the normal flow level and to ensure⁹⁶⁶
 966 working to restore the normal flow level and to ensure⁹⁶⁷
 967 working to restore the normal flow level and to ensure⁹⁶⁸
 968 working to restore the normal flow level and to ensure⁹⁶⁹
 969 working to restore the normal flow level and to ensure⁹⁷⁰
 970 working to restore the normal flow level and to ensure⁹⁷¹
 971 working to restore the normal flow level and to ensure⁹⁷²
 972 working to restore the normal flow level and to ensure⁹⁷³
 973 working to restore the normal flow level and to ensure⁹⁷⁴
 974 working to restore the normal flow level and to ensure⁹⁷⁵
 975 working to restore the normal flow level and to ensure⁹⁷⁶
 976 working to restore the normal flow level and to ensure⁹⁷⁷
 977 working to restore the normal flow level and to ensure⁹⁷⁸
 978 working to restore the normal flow level and to ensure⁹⁷⁹
 979 working to restore the normal flow level and to ensure⁹⁸⁰
 980 working to restore the normal flow level and to ensure⁹⁸¹
 981 working to restore the normal flow level and to ensure⁹⁸²
 982 working to restore the normal flow level and to ensure⁹⁸³
 983 working to restore the normal flow level and to ensure⁹⁸⁴
 984 working to restore the normal flow level and to ensure⁹⁸⁵
 985 working to restore the normal flow level and to ensure⁹⁸⁶
 986 working to restore the normal flow level and to ensure⁹⁸⁷
 987 working to restore the normal flow level and to ensure⁹⁸⁸
 988 working to restore the normal flow level and to ensure⁹⁸⁹
 989 working to restore the normal flow level and to ensure⁹⁹⁰
 990 working to restore the normal flow level and to ensure⁹⁹¹
 991 working to restore the normal flow level and to ensure⁹⁹²
 992 working to restore the normal flow level and to ensure⁹⁹³
 993 working to restore the normal flow level and to ensure⁹⁹⁴
 994 working to restore the normal flow level and to ensure⁹⁹⁵
 995 working to restore the normal flow level and to ensure⁹⁹⁶
 996 working to restore the normal flow level and to ensure⁹⁹⁷
 997 working to restore the normal flow level and to ensure⁹⁹⁸
 998 working to restore the normal flow level and to ensure⁹⁹⁹
 999 working to restore the normal flow level and to ensure⁹⁹⁹

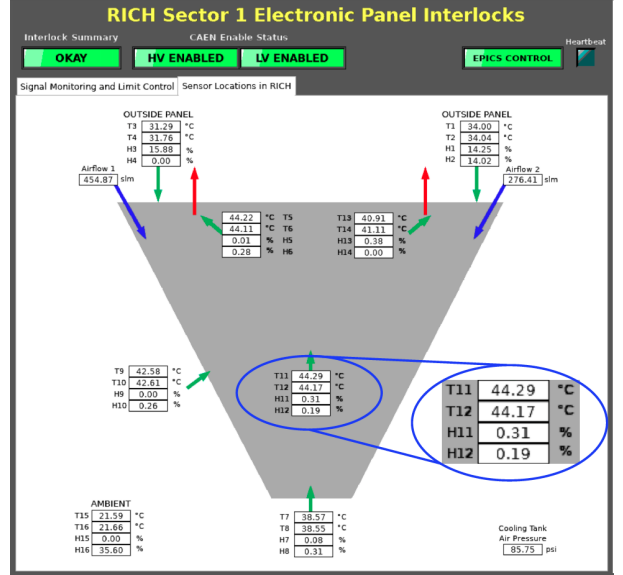


Figure 31: Location and measured values of the temperature and humidity sensors inside the electronics panel, and the cooling air input flow as measured by the flow meters of the gas line.

safe humidity conditions. During RICH operation, the humidity level has proven to be very stable with time.

5. The Initial Performance of the RICH Detector

5.1. RICH Event Reconstruction

The RICH reconstruction is organized in four steps. In the first step, the spatial and time information of each hit in the MaPMTs is corrected by the spatial misalignment and time calibration parameters. The hits are ordered as a function of their ToT value, as this reflects the corresponding amplitude (released charge). A 3×3 MaPMT pixel matrix centered around a local maximum, i.e. the hit with the highest local ToT, is called a nonet. If more than 3 hits are found in the same nonet they are grouped into a RICH cluster. A cluster is typically generated by a charged particle producing Cherenkov light in the MaPMT window or ionization in the sensor dynode structure. If a sole hit is found close to a local maximum with a ToT lower than 80% of that maximum, the hit is flagged as possible cross-talk. Hits belonging to the same nonet of the local maximum are flagged as optical cross-talk, while hits readout by an electronics channel adjacent to the maximum hit in the MAROC chip are flagged as electrical cross-talk. Note that the readout circuit routing has been designed to connect anodes close in space to non-adjacent MAROC3 inputs. The above selection rejects about 87% of the cross-talk hits, as can be seen in Fig. 34. In the figure, the ToT distribution of the recorded RICH hits (black solid line) is shown together with the distributions of the hits identified as optical (magenta dash-dotted line) or electrical (green dashed line) cross-talk. The

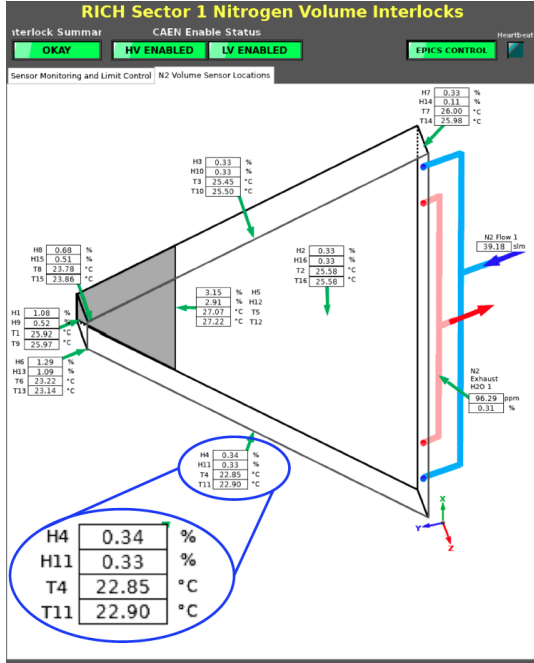


Figure 32: Location and measured values of the temperature and humidity sensors inside the nitrogen volume, and the nitrogen input flow as measured by the flow meters of the gas line.

shoulders on the right of the cross-talk peaks are likely due to signal discharges wrongly identified as cross-talk. The hits selected for further analysis are highlighted by the dotted (blue) histogram. The excess at low ToT values indicates a residual contamination of unidentified cross-talk. The leftover cross-talk contamination, at the level of 2.7% of the signal, can be further reduced only with a time versus amplitude analysis, see Section 5.2. The cross-talk selection also removes a small (0.8% fraction) of true Cherenkov signals. Those correspond to MaPMT discharges that undergo incomplete dynode multiplication, while being by chance close in space to another Cherenkov signal. Hits flagged as cross-talk are not considered further in the RICH reconstruction.

The second step consists in finding the spatial match between the RICH clusters and the CLAS12 charged particle tracks. This requires that the extrapolated impact point of the track on the MaPMT plane is within 10 cm of the cluster center. The latter is calculated as a weighted average - with the ToT value as the weight - of the spatial coordinates of all the hits in the cluster. Matched clusters allow a precise study of the MaPMT detector position and orientation relative to the CLAS12 tracking system. This is shown in Fig. 35, where the distance between the RICH clusters and the matched drift chamber tracks [24] divided by the pixel spatial RMS, a sort of χ^2 distribution, is reported. The black distribution is before and the red one is after the alignment procedure.

The third step is the core of the RICH reconstruction [25]. For each hit in the MaPMT plane, an

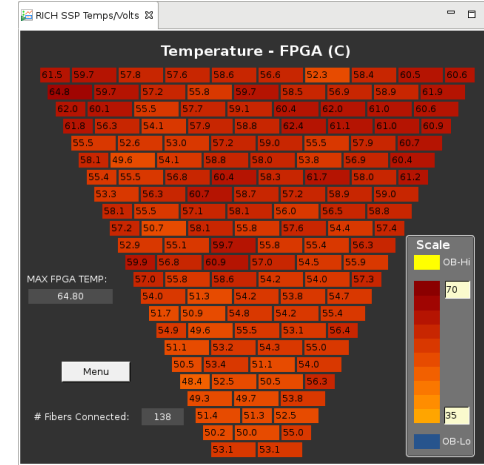


Figure 33: Slow controls display: Map of the temperatures measured on the FPGA chips.

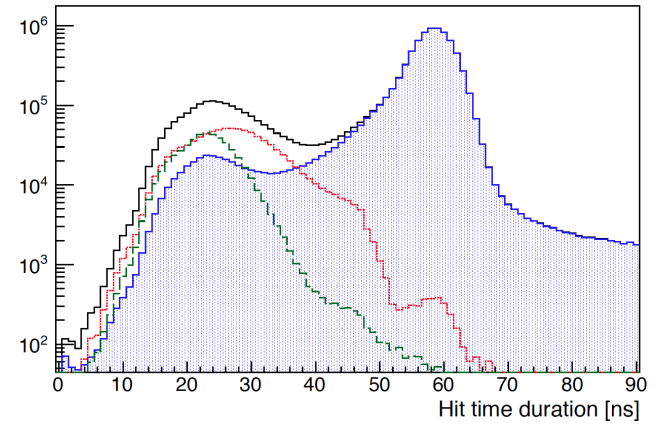


Figure 34: ToT distribution of the recorded RICH hits (black solid line) together with the optical (magenta dash-dotted line) and electrical (green dashed line) cross-talk distributions. The hits selected for further analysis are highlighted by the blue dotted histogram.

estimate of the corresponding Cherenkov angle is derived by ray-tracing the photon path inside the RICH volume taking into account possible reflections. This is done in turn for each charged particle traced through the RICH, with the photon emission point assumed to be the middle point of the particle path inside the aerogel radiator. In the fourth step, a particle identification algorithm is applied using an event-based likelihood of the reconstructed Cherenkov angles and times.

5.2. RICH Time Resolution

The time information of the RICH hits is provided by the leading edge time T_1 measured by the TDC implemented into the FPGA board with a 1-ns precision. In-time photon hits are selected by comparing their T_1 with the time T_{calc} computed using the CLAS12 information (see Fig. 36). T_{calc} comprises the event start time, the

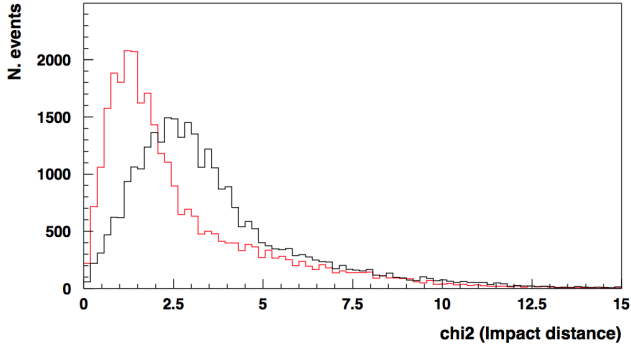


Figure 35: RICH matching χ^2 , defined as the distance between the RICH clusters and the matched drift chamber tracks divided by the pixel spatial RMS. The black distribution is before and the red one is after the alignment procedure.

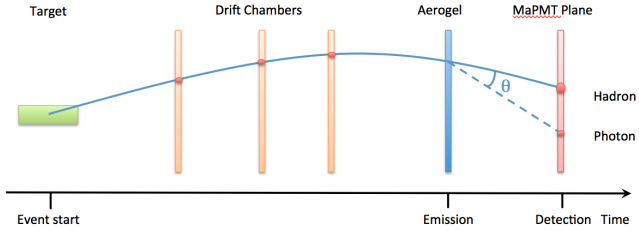


Figure 36: The RICH photon detection time as measured by the CLAS12 spectrometer. It is defined as the event start time plus the flight-times of the hadron from the interaction point to the radiator center and of the ray-traced photon within the RICH volume.

862 charged track path and flight time provided by the tracking
 863 system, and the Cherenkov photon path reconstructed
 864 inside the RICH as explained in Ref. [25]. Being based
 865 on the precise FTOF system [3] and the accelerator RF⁸⁸⁸
 866 frequency, the CLAS12 computed time features a time⁸⁸⁹
 867 resolution on the order of 100 ps, significantly better than⁸⁹⁰
 868 RICH. The CLAS12 computed time can therefore be used⁸⁹¹
 869 as a reference for the RICH time calibration.⁸⁹²

870 With respect to the expected time resolution, significant⁸⁹³
 871 channel-by-channel variations are found in the difference⁸⁹⁴
 872 between the measured and the calculated times as shown⁸⁹⁵
 873 in the top plot of Fig. 37, where the distribution of $\Delta T = ^{896}$
 874 $T_1 - T_{calc}$ as a function of the channel number is shown.⁸⁹⁷
 875 These variations are introduced by the readout chain, with⁸⁹⁸
 876 the biggest contribution coming from the average length of⁸⁹⁹
 877 the 3 optical DAQ fiber trunks and from the specific length⁹⁰⁰
 878 of the various fibers in each trunk. Smaller variations⁹⁰¹
 879 among the individual channels of one board can also⁹⁰²
 880 occur due to the different circuit routing and components.⁹⁰³
 881 An additional overall time constant is expected from the⁹⁰⁴
 882 relative calibration of the RICH with respect to the rest⁹⁰⁵
 883 of the CLAS12 detectors.⁹⁰⁶

884 A broadening of the ΔT distributions is due to the time⁹⁰⁷
 885 walk, i.e. the dependence of the trailing edge time on⁹⁰⁸
 886 the amplitude of the input signal. Since the MAROC⁹⁰⁹
 887 readout mostly works in the saturated regime already⁹¹⁰

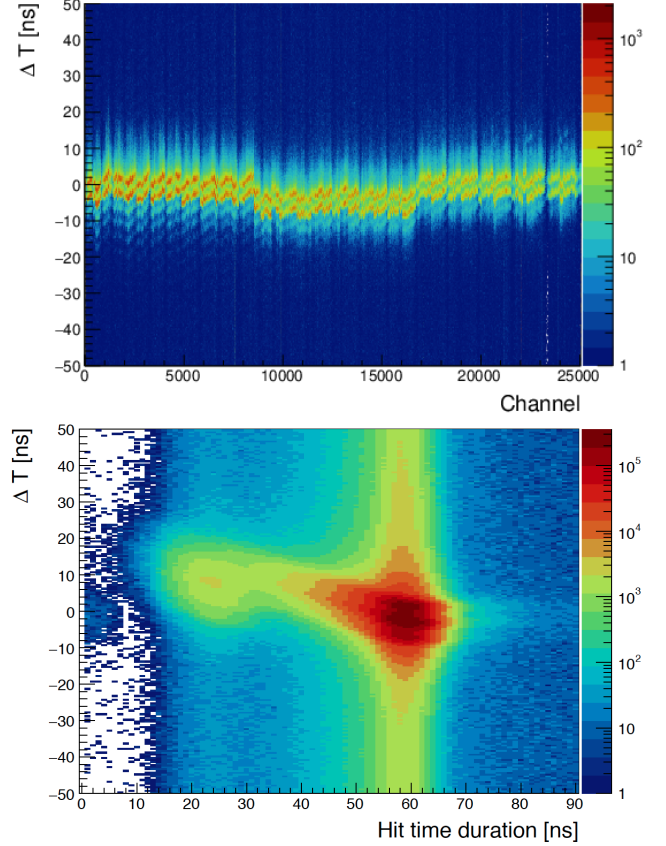


Figure 37: Top plot: distribution of the time difference ΔT between the measured RICH and calculated CLAS12 times as a function of the RICH readout channel. Bottom plot: cumulative distribution of the time difference ΔT as a function of the hit duration time (ToT).

at the SPE level, this effect is expected to be relevant for small amplitude signals, as can be seen from the bottom plot of Fig. 37. Saturated signals have typical ToT values on the order of 60 ns, while small amplitude signals are expected to be discriminated up to several ns later. The vertical band at $ToT \approx 60$ ns comprises a distribution of random-time MaPMT dark counts and off-time beam bunches. The independent excess around $ToT \approx 25$ ns signals a residual contamination of cross-talk pulses anticipated in Section 5.1.

A two-step calibration procedure was implemented in order to align the time measured from all RICH readout channels with the expected (calculated) one. The current version of the software uses electrons and charged pions identified in CLAS12 with momenta larger than 2.5 GeV and Cherenkov photons reconstructed in the RICH with no reflections on the mirrors.

The first step of the procedure consists in the evaluation of the 25024 time offset corrections. The values of ΔT are plotted for each channel and the position of the maximum is taken as the time offset for that channel. The top plot of Fig. 38 shows a typical ΔT distribution, with a pronounced peak, a broad tail due to the time walk,

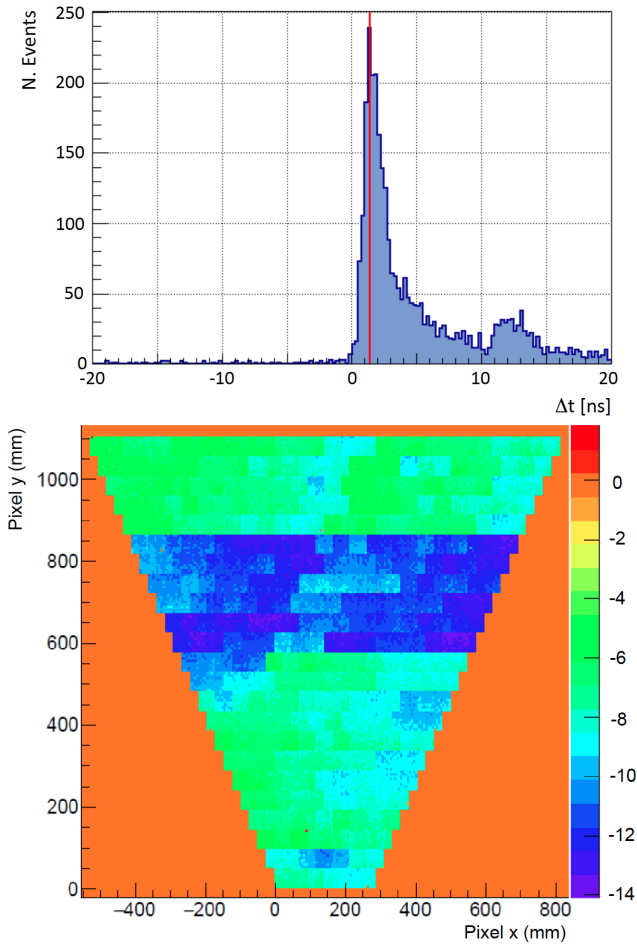


Figure 38: Top plot: ΔT distribution for one readout channel; the red line indicates the time offset value. Bottom plot: typical map of ΔT for one MaPMT.

933
934
935

911 and a small enhancement above ≈ 10 ns most likely due₉₃₆
912 to residual cross-talk hits. The vertical line indicates₉₃₇
913 the adopted value for the time offset correction. The₉₃₈
914 bottom plot of Fig. 38 shows a typical map of the₉₃₉
915 time offsets. Three regions of comparable values are₉₄₀
916 highlighted, corresponding to the tiles connected to the₉₄₁
917 optical fiber trunks, on top of smaller channel-by-channel₉₄₂
918 variations.

943

919 Once the individual channels were corrected for the time₉₄₄
920 offsets, the time-walk corrections were extracted from the₉₄₅
921 ΔT distribution as a function of ToT. Since the threshold₉₄₆
922 level is common to all channels of one MAROC3 chip,₉₄₇
923 and the amplitude equalization has been performed, one₉₄₈
924 expects that the same time-walk correction should work₉₄₉
925 for all channels of one MaPMT. This was verified by₉₅₀
926 comparing plots like the one shown in the bottom plot₉₅₁
927 of Fig. 37 for all channels of the MaPMTs. A set of₉₅₂
928 391 time-walk correction functions, one per MaPMT, is₉₅₃
929 therefore extracted by fitting the dependence of ΔT as₉₅₄
930 a function of ToT, as shown in the top plot of Fig. 39.₉₅₅
931 The dependence is fit with two lines, one for the saturated₉₅₆

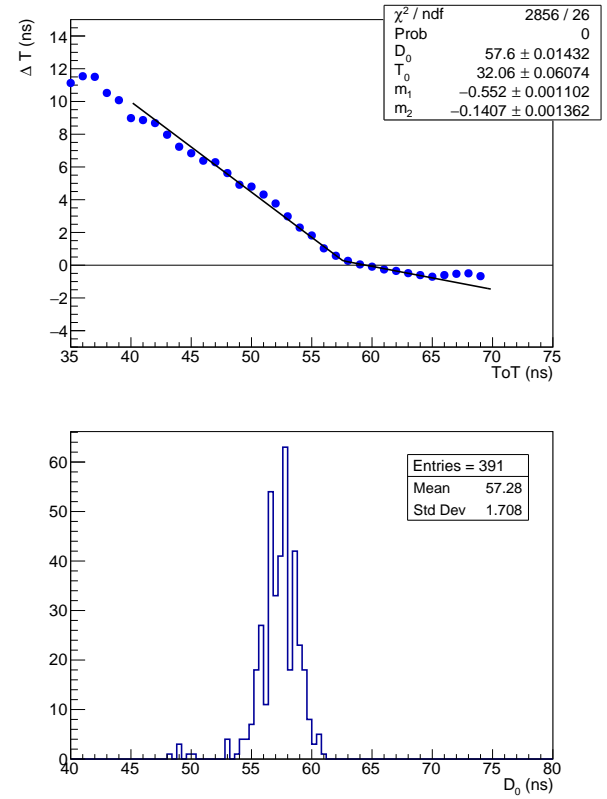


Figure 39: Top plot: fit of the time-walk correction for one MaPMT. Bottom plot: distribution of the ToT saturation values extracted from the time-walk corrections.

regime and one for the linear region. The free parameters of the fit are the two slopes, the ToT value where the two lines cross, i.e. the saturation ToT, and the ΔT at zero ToT. The data show small deviations from the linear behavior. However, such a simple functional form was adopted to minimize the probability of fit failure (having to deal with several hundreds of fits) and because it was proven to be enough to achieve time resolutions that meet the specifications. In the bottom plot of Fig. 39, a typical distribution of the saturation ToT values obtained from the fit is shown. The average value is around 57 ns with small variation from MaPMT to MaPMT.

After calibration, the corrected ΔT distribution is centered at zero for all channels, see Fig. 40. As a consequence, a few ns time coincidence can be applied to remove the spurious hits. As shown in the bottom panel of Fig. 40, the cross-talk hits at $ToT \approx 25$ ns and the 4.008 ns sub-structure of the off-time beam bunches at $ToT \approx 60$ ns become clearly visible. A typical ΔT distribution is shown for one MaPMT in Fig. 41, where the red and black histograms show the ΔT values before and after the correction, respectively. The red curve is a Gaussian fit of the corrected distribution. On average, we obtained a time resolution $\langle \sigma \rangle \approx 0.7$ ns, well below the requirement of 1 ns.

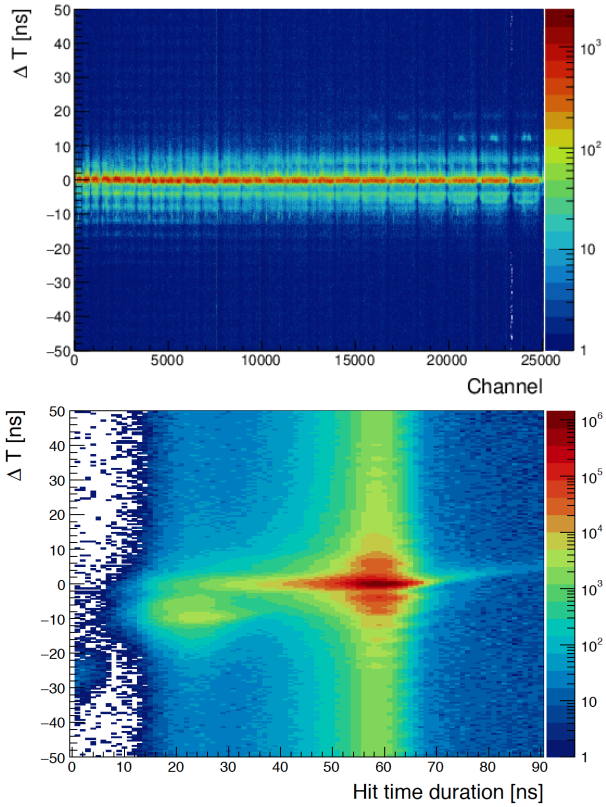


Figure 40: Distribution of the time difference ΔT between the measured RICH and extrapolated CLAS12 times after the time calibration. On the top as a function of the readout channel; on the bottom as a function of the signal amplitude ToT.

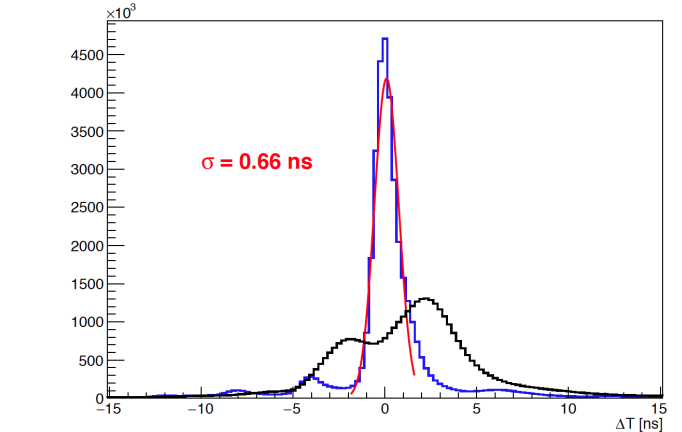


Figure 41: Typical ΔT distribution before (black) and after (blue) the time-walk correction for all RICH pixels. The red line is a Gaussian fit of the corrected distribution, with a global width $\sigma=0.66$ ns

photodetectors, indicated by the small dots in the figures. The measured RICH hits are shown as open circles, whereas the reconstructed photon hits are shown as the full circles. Direct and reflected photons are indicated in magenta and blue, respectively. A remarkable feature of the RICH detector is the low level of spurious hits from accidentals, in-time background (i.e. Rayleigh scattering), and dark counts. This feature is crucial for the most challenging cases: particles with high momenta close to the 8 GeV limit that require the best resolution in Cherenkov angle, and particles pointing towards the spherical mirror whose number of detected photons is limited by the double reflection and a second passage through the radiator.

For each event, the details of the time and Cherenkov angle reconstruction are shown on the right. On the top panel, the time coincidence ΔT between the RICH measured hit and the CLAS12 calculated time is displayed as a function of the photon flight time within the RICH (photon transit time). The time coincidence ΔT should be close to zero for any true photon path. As a consequence, a valid photon reconstruction is initially selected by requiring $\Delta T < 3$ ns, indicated by the horizontal dashed lines. The path length is represented by the photon transit time inside the RICH, from the emission point within the aerogel to the detection point in the MaPMT plane after all possible reflections. Photons reflected by the spherical mirror and directed back to the aerogel travel twice the gap, with an expected significant increase of path length and a corresponding distinctive ≈ 6 ns longer transit time.

In the bottom panel, the measured angles are compared to the expected distributions for different particle hypotheses. The width of each distribution corresponds to the expected SPE angular resolution, while the average value depends on the particle type and momentum. An acceptance range is defined from the smallest angle expected for a proton to the largest angle expected for

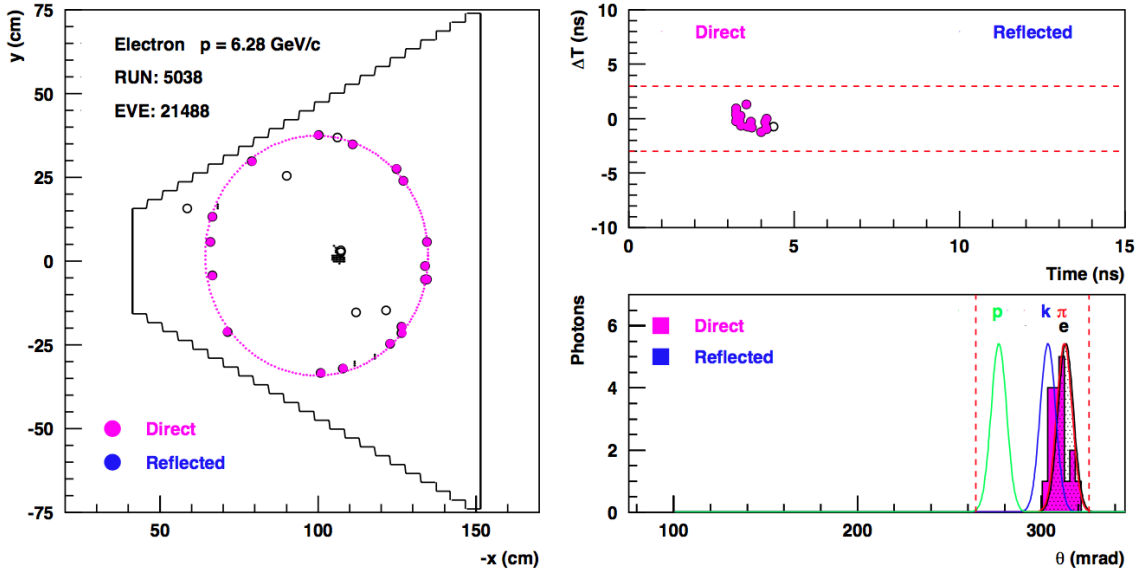


Figure 42: Example of a reconstructed RICH event with only direct photons. On the left the event display, on the right the time (top) and angle (bottom) analysis. Refer to the text for details.

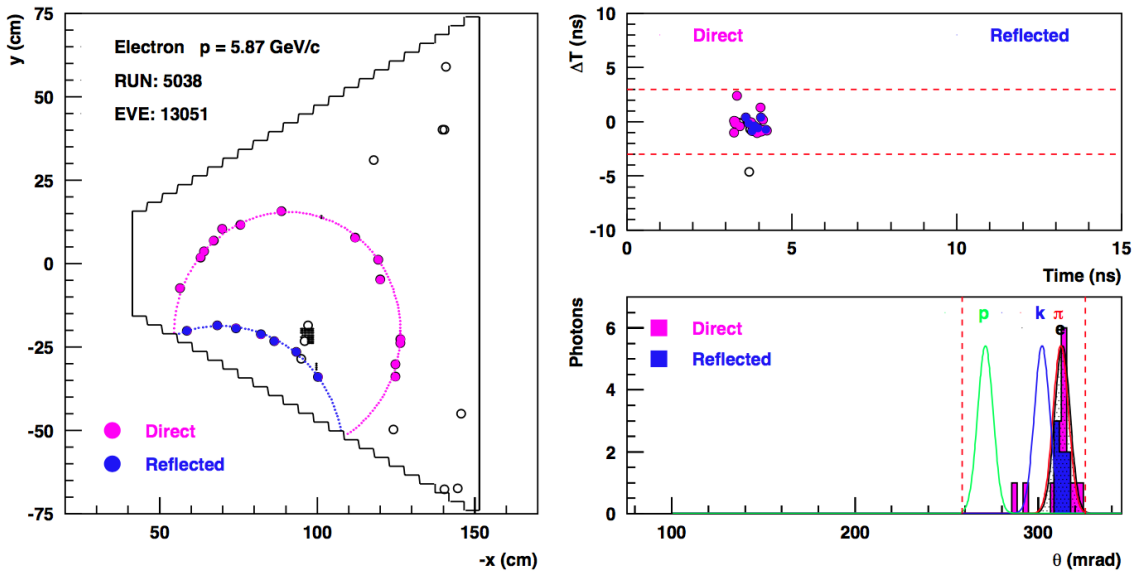


Figure 43: Example of a reconstructed RICH event with a partial ring reflected by the lateral flat mirror. On the left the event display, on the right the time (top) and angle (bottom) analysis. Refer to the text for details.

1018 an electron, enlarged by three times the expected angular resolution. For the latter, a conservative value of 6 mrad is taken for the single photon case. These limits are indicated by the vertical dashed lines.

1022 For each reconstructed photon path an estimate of the corresponding Cherenkov angle is obtained and histogrammed on the plot. In all cases studied, both reflected and direct photon information is consistent with the electron hypothesis. In particular, the reconstructed reflected and direct photon paths with ΔT close to zero provide Cherenkov angle values consistent with an

electron, as expected. The narrow distribution of the measured angle values indicate that kaons can clearly be separated up to momenta greater than 6 GeV. Electrons can be distinguished from pions only at low momenta, below 2 GeV.

Each aerogel tile presents specific features because the challenging production process, tuned to achieve the highest transparency over a large volume, is not fully industrialized. The most important quality parameters are the density, related to the average refractive index, homogeneity, related to the refractive index variations

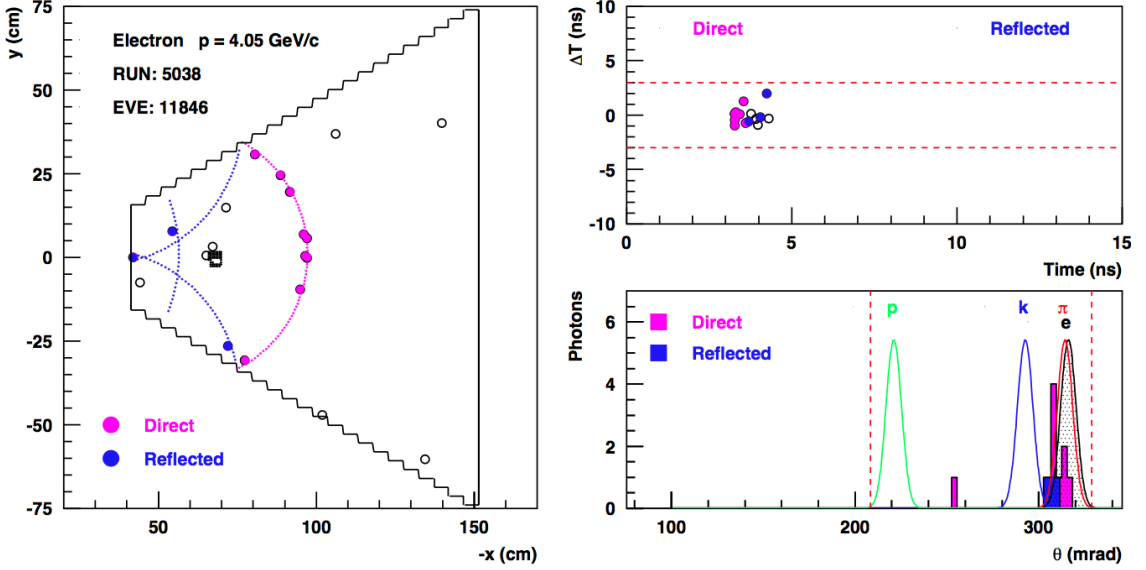


Figure 44: Example of a reconstructed RICH event with photons reflected by all the lateral mirrors. On the left the event display, on the right the time (top) and angle (bottom) analysis. Refer to the text for details.

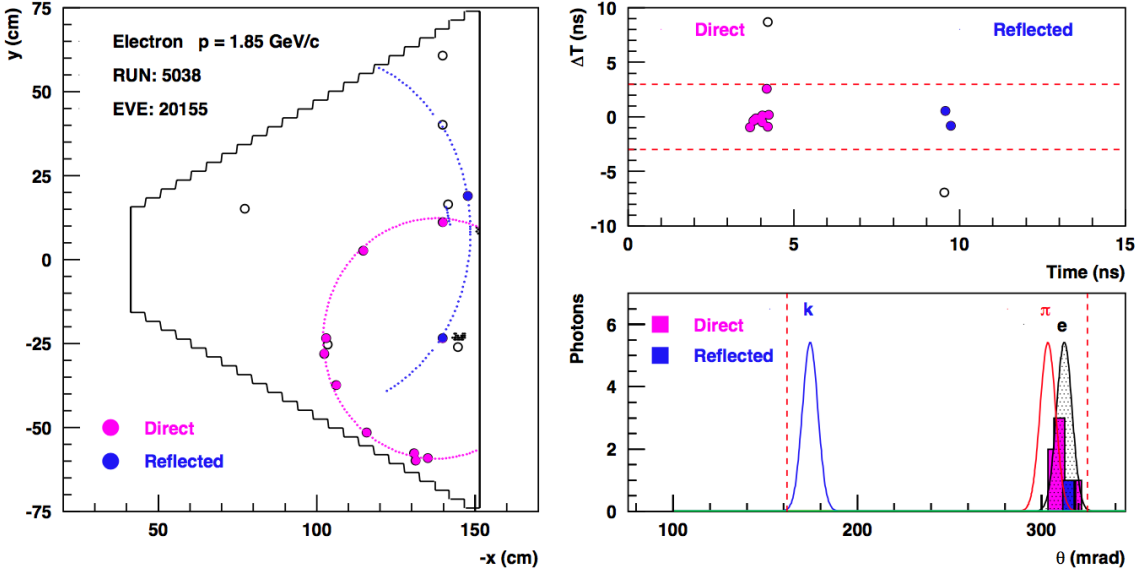


Figure 45: Example of a reconstructed RICH event with a partial ring reflected back by the spherical mirror and passing twice the aerogel layer. On the left the event display, on the right the time (top) and angle (bottom) analysis. Refer to the text for details.

within the volume, and tile bending, originated by the inner material tension and related to the surface planarity. The effect of these features on the RICH photon reconstruction can be studied in detail using the control sample of electrons identified by CLAS12. Given the large number of tiles and the broad range of particle directions after the CLAS12 bending magnets, such a study requires large statistics and is still ongoing. A similar approach is used for the alignment study. Also in this case, large statistics are needed due to the numerous involved components (aerogel layers, mirrors, and MaPMT plane) and photon

path configurations.

As a general approach, the RICH performance is studied separately for each aerogel tile. The RICH global performance estimators are then defined by averaging the results over all the radiator tiles. Despite the fact that the above studies have not yet been finalized, and only partial corrections have been implemented so far, the preliminary SPE Cherenkov angle resolution yields typical values around 6 mrad. It is expected to improve towards the goal value of 4.5 mrad once the corrections for the detector misalignment are implemented and the

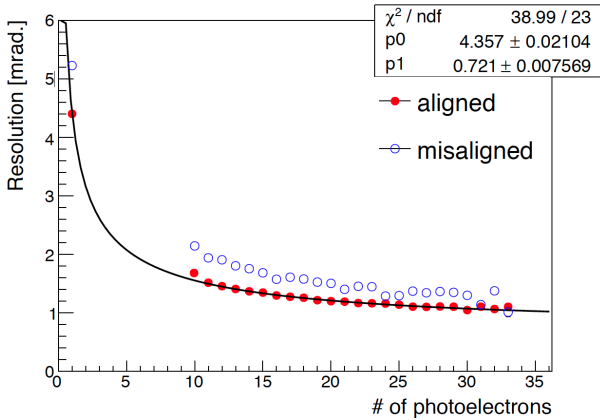


Figure 46: RICH Cherenkov resolution before (open points) and after (solid points) a preliminary RICH alignment. The whole RICH detector is aligned minimizing the matching distance between the RICH clusters and the extrapolated drift chamber tracks. No possible misalignment of a single RICH component is accounted for. The distribution is for particles passing through one aerogel tile of 2-cm thickness (tile 12 in layer 1) and for direct photons.

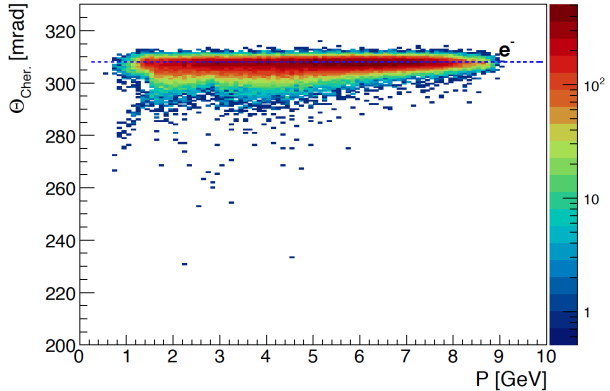


Figure 47: RICH response for electrons as identified by CLAS12. As expected, the measured Cherenkov angle is saturated over the whole momentum range, from 3 GeV up to 8 GeV. The distribution is for particles passing through one aerogel tile of 2-cm thickness (tile 12 in layer 1) and direct photons.

realistic optical parameters of each aerogel tile are taken¹⁰⁸²
into account.¹⁰⁸³

As an example, the effect of a preliminary alignment of¹⁰⁸⁴ the RICH as a whole is shown for one aerogel tile in Fig. 46¹⁰⁸⁵. The resolution is calculated as the RMS of the distribution¹⁰⁸⁶ of the average Cherenkov angles extracted for each single¹⁰⁸⁷ track of the electron control sample. Such averages are¹⁰⁸⁸ calculated over the detected photons, whose reconstructed¹⁰⁸⁹ path satisfies the time coincidence and provides an angle¹⁰⁹⁰ within the kinematic limits described above, associated¹⁰⁹¹ with the track. The fit shown uses the function¹⁰⁹²

$$\sigma = \sqrt{\frac{\sigma_1^2}{N} + \sigma_0^2}$$

to extract the single photon resolution σ_1 in addition to a¹⁰⁹³ constant term σ_0 measuring the residual systematics due¹⁰⁹⁴, e.g. to misalignment. After alignment, the resolution¹⁰⁹⁵ improves toward the design values, which are 4.5 mrad¹⁰⁹⁶ for single photon detection and 1.5 mrad for the average¹⁰⁹⁷ over all the photons that are associated with the control¹⁰⁹⁸ electron track. Such preliminary Cherenkov angle resolu-¹⁰⁹⁹ tion is already sufficient for an effective hadron separation¹¹⁰⁰ in the goal range of momenta, from 3 to 8 GeV, as shown¹¹⁰¹ by Figs. 47 to 49.¹¹⁰²

6. Conclusions

A RICH detector has been designed to enhance the¹¹² hadron identification capability at CLAS12 in the 3 to 8₁₁₃ GeV momentum range. It substitutes the baseline LTCG₁₁₄ gas threshold Cherenkov detector in two of the CLAS12₁₁₅ sectors, to create a symmetric left-right setup optimized₁₁₆ for running with polarized targets. The first module was₁₁₇ installed at the beginning of 2018, in time for the start of₁₁₈

the experiment data taking. The second module is under construction and expected to be ready in the summer 2021, in time for the first run with polarized targets.

To efficiently cover the desired few-GeV momentum range, the RICH employs innovative technological solutions. Among these are composite aeronautic light-materials to ensure the needed mechanical structure rigidity, aerogel radiators of unprecedented large volume (up to $200 \times 200 \times 30 \text{ mm}^3$) and high transparency ($\approx 50 \text{ mm}$ scattering length), light mirrors (of the order of 1% radiation length) made of carbon fiber or, for the first time in a nuclear experiment, glass-skin technology, and highly segmented and highly packed Hamamatsu H8500 and H12700 multi-anode photomultipliers. A compact and scalable readout electronics system has been realized for the detector, able to discriminate Cherenkov signals down to as small as a 1/32 fraction of the single photon amplitude, with excellent efficiency and stability, and a time resolution better than 1 ns.

The peculiar geometry of the CLAS12 sector suggested a innovative hybrid-optics solution to limit the active area to $\approx 1 \text{ m}^2$ per sector, with part of the light directly imaged and part of the light detected after reflection from mirrors. This and the bending into the torus field of the CLAS12 Forward Detector create a variety of possible topologies for the particle and photons paths. The RICH reconstruction exploits a ray-tracing algorithm to provide a Cherenkov angle estimation for each photon hit and hadron track in the event. This basic experimental information allows an independent development of higher-level PID algorithms with increasing sophistication.

Preliminary data analysis shows that the CLAS12 RICH is able to match the required time and Cherenkov angle resolutions. After calibration, each of the 25k channels features a time resolution of the order of 0.6 ns, better than the 1 ns specification. High-momentum particles define the most stringent requirements for the RICH performance.

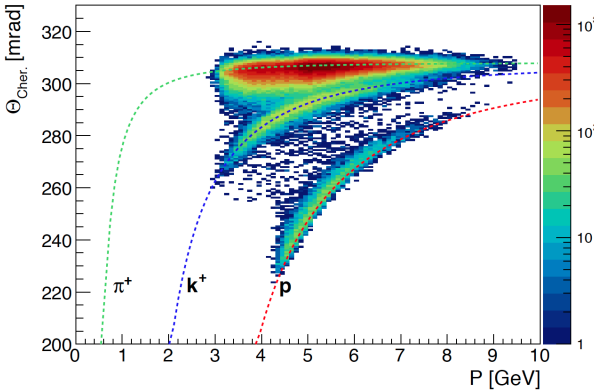


Figure 48: RICH response for non-electron particles as defined by CLAS12. The measured Cherenkov angles distribute around the expected values for pion, kaon, and proton hypotheses as a function of their momentum. The three hadron populations are separated over the whole momentum range, from 3 GeV up to 8 GeV. The distribution is for particles passing through one aerogel tile of 2-cm thickness (tile 12 in layer 1) and spanning the entire momentum range of interest for RICH.

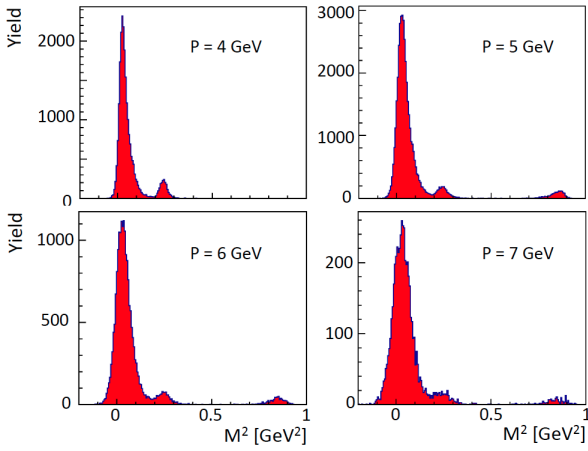


Figure 49: RICH response for non-electron particles in slices of momentum, from 4 GeV up to 7 GeV.

As the pion yield is larger than the other particles species by an order of magnitude, a 4σ angle separation is required to contain the contamination at the percent level. At 8 GeV, this implies an angle resolution of 1.5 mrad. Despite the fact that the detailed study of the alignment and optical performance of the various components is still ongoing, the detector has already demonstrated a single-photon angle resolution better than 5 mrad and an average number of 19 photons per charged particle in the forward high-momentum direction, in line with the detector design specifications. This reflects in an angle resolution per charged particle close to the design value of 1.5 mrad and an effective hadron identification capability over the entire required momentum range.

7. Acknowledgments

This material is based upon work supported by INFN under the MIUR priority project CLASMED, Italy and by the U.S. Department of Energy, Office of Science, Office of Nuclear Physics under contract DE-AC05-06OR23177 and the National Science Foundation, Award #1615067. We thank the JLab Detector Support Group and Fast Electronics Group, the Hall B technical and management staff, and the INFN technical and administrative service.

References

- [1] Y. Sharabian *et al.*, “The CLAS12 High Threshold Cherenkov Counter”, to be published in Nucl. Inst. and Meth. A, (2020). (see this issue)
- [2] M. Ungaro *et al.*, “The CLAS12 Low Threshold Cherenkov Counter”, to be published in Nucl. Inst. and Meth. A, (2020). (see this issue)
- [3] D.S. Carman *et al.*, “The CLAS12 Forward Time-of-Flight System”, to be published in Nucl. Inst. and Meth. A, (2020). (see this issue)
- [4] V.D. Burkert *et al.*, “The CLAS12 Spectrometer at Jefferson Laboratory”, to be published in Nucl. Inst. and Meth. A, (2020). (see this issue)
- [5] G. Asryan *et al.*, “The CLAS12 Forward Electromagnetic Calorimeter”, to be published in Nucl. Inst. and Meth. A, (2020). (see this issue)
- [6] M. Contalbrigo *et al.*, “The Large-Area Hybrid-optics CLAS12 RICH Detector: Tests of Innovative Components”, Nucl. Inst. Meth. **A766**, 22 (2014).
- [7] M. Contalbrigo *et al.*, “Aerogel mass production for the CLAS12 RICH: Novel characterization methods and optical performance”, Nucl. Inst. Meth. **A876**, 168 (2017).
- [8] E. Aschenauer *et al.*, “Optical Characterization of $n = 1.03$ Silica Aerogel used as Radiator in the RICH of HERMES”, Nucl. Inst. Meth. **A 440**, 338 (2000).
- [9] <http://www.compositemirrors.com/>.
- [10] G.J. Barber *et al.*, “Development of Lightweight Carbon-Fiber Mirrors for the RICH 1 Detector of LHCb”, Nucl. Inst. Meth. **A593**, 624 (2008).
- [11] <https://www.evaporatedcoatings.com/>.
- [12] <http://www.media-lario.com/>.
- [13] https://www.hamamatsu.com/resources/pdf/etd/H8500_H10966 TPMH1327E.pdf.
- [14] R. A. Montgomery *et al.*, “Multianode Photomultiplier Tube Studies for Imaging Applications”, Nucl. Inst. Meth. **A 695**, 326 (2012).
- [15] S. Anefalos Pereira *et al.*, “Test of the CLAS12 RICH Large Scale Prototype in the Direct Proximity Focusing Configuration”, Eur. Phys. J. A **52**, 23 (2016).
- [16] <https://www.hamamatsu.com/resources/pdf/etd/H12700 TPMH1348E.pdf>.
- [17] M. Contalbrigo *et al.*, “Single Photon Detection with the Multi-anode CLAS12 RICH Detector”, in press in Nucl. Inst. Meth. A., DOI:10.1016/j.nima.2019.04.077
- [18] S. Blin *et al.*, “MAROC, a Generic Photomultiplier Readout Chip”, IEEE Nucl. Sci. Symp. Conf. Rec. 2010, 1690 (2010).
- [19] S. Boyarinov *et al.*, “The CLAS12 Data Acquisition System”, to be published in Nucl. Inst. and Meth. A, (2020). (see this issue)
- [20] Pavel Degtiarenko, “Precision Analysis of the Photomultiplier Response to Ultra Low Signals”, Nucl. Inst. Meth. **A872**, 1 (2017).
- [21] P. Degtiarenko, V. Kubarovskiy, A. Kim, and A. Smith, to be published.
- [22] Experimental Industrial Physics Control System, <https://epics-controls.org>

- 1198 [23] https://www.jlab.org/div_dept/physics_division/dsg/notes/2016-012%20National%20Instruments%20compactRIO-based%20control,%20monitoring,%20and%20interlock%20system.pdf
- 1199
1200
1201
1202 [24] M.D. Mestayer *et al.*, “*The CLAS12 Drift Chamber System*”,
1203 to be published in Nucl. Inst. and Meth. A, (2020). (see this
1204 issue)
1205 [25] V. Ziegler *et al.*, “*The CLAS12 Software Framework and Event*
1206 *Reconstruction*”, to be published in Nucl. Inst. and Meth. A,
1207 (2020). (see this issue)